The interaction between Gravity Waves and Solar Tides: Results from *4D* Ray Tracing coupled to a Linear Tidal Model

B. Ribstein,[1] U. Achatz[1] and F. Senf[2]

Corresponding author: B. Ribstein, Institut für Atmosphäre und Umwelt, Johann Wolfgang Goethe Universität Frankfurt, Altenhöferallee 1, Germany. ribstein@iau.uni-frankfurt.de

[1]Institut für Atmosphäre und Umwelt,

Johann Wolfgang Goethe Universität

Frankfurt, Frankfurt-am-Main, Germany.

[2]Leibniz Institute for Tropospheric

Research, Leipzig, Germany.

Abstract. The interaction between solar tides (STs) and gravity waves (GWs) is studied via the coupling of a three-dimensional ray-tracer model and a linear tidal model. The ray-tracer model describes GW dynamics on a spatially and time dependent background formed by a monthly mean climatology and STs. It does not suffer from typical simplifications of conventional GW parameterizations where horizontal GW propagation and the effects of horizontal background gradients on GW dynamics are neglected. The ray-tracer model uses a variant of *Wentzel-Kramers-Brillouin* (WKB) theory where a spectral description in position-wavenumber space is helping to avoid numerical instabilities otherwise likely to occur in caustic-like situations. The tidal model has been obtained by linearization of the primitive equations about a monthly mean, allowing for stationary planetary waves. The communication between ray-tracer model and tidal model is facilitated using latitude and altitude-dependent coefficients, named Rayleigh-friction and Newtonian-relaxation, and obtained from regressing GW momentum and buoyancy fluxes against the STs and their tendencies. These coefficients are calculated by the ray-tracer model and then implemented into the tidal model. An iterative procedure updates successively the GW fields and the tidal fields until convergence is reached. Notwithstanding the simplicity of the employed GW source many aspects of observed tidal dynamics are reproduced. It is shown that the conventional *"single-column"* approximation leads to significantly overestimated GW fluxes and hence underestimated ST amplitudes, pointing at a sensitive issue of GW parameterizations in general.

1. Introduction

Solar tides (STs) are atmospheric global-scale waves induced by the daily cycle of solar radiation. STs and internal gravity waves (GWs) are primarily excited in the troposphere and lower-stratosphere, before they propagate upwards. They transport energy, momentum and entropy from high to low density regions. Due to nearly exponential growth in the ascendant motion, GWs and STs strongly influence the dynamics and circulation of the middle-atmosphere. They are considered to be one of the main constituents of the dynamical coupling between the troposphere and the mesosphere and lower-thermosphere (MLT), even if planetary waves also play an important role, for example Rossby waves on the dynamics of the stratosphere.

GW sources include topography, deep convection, latent heat release and wind shear, although wave breaking, wave-wave interactions and the adjustment of unbalanced flows also contribute, see the review by *Fritts and Alexander* [2003]. These different sources vary seasonally and geographically and the associated spectrum is expected to exhibit a wide range of frequencies and wavelengths, see e.g. the work on non-orographic gravity sources parameterizations [e.g. *Buhler and McIntyre*, 1999a; *Song and Chun*, 2005; *Choi and Chun*, 2011; *de la Camara et al.*, 2014; *de la Camara and Lott*, 2015]. The altitude of GW breaking depends on the GW characteristics and on the atmospheric conditions during the propagation. The altitude can be either in the middle-atmosphere or in even higher regions where molecular dissipation matters, e.g. *Buhler and McIntyre* [1999b], *Vadas and Fritts* [2005, 2006] and *Vadas* [2013]. GW breaking is associated with a deposition of energy, momentum and entropy.

GW breaking leads to a forcing of the surrounding flow. Major GW effects arise from wave-mean flow interactions. GW mean-flow forcing explains the closure of the jets in the mesosphere, the residual circulation from summer to winter hemisphere near the mesopause and a cooling (warming) in the summer (winter) hemisphere [e.g. *Lindzen*, 1981; *Holton*, 1982; *Dunkerton and Butchart*, 1984]. The influence of GWs on the mean flow varies due to seasonal variations of middle-atmosphere condition. Since the influence of STs varies seasonally, the contribution of GWs to the transient flow [e.g. *Walterscheid*, 1981; *Ortland and Alexander*, 2006; *Senf and Achatz*, 2011] must vary seasonally as well. But effects from GW transient-flow interaction are less established.

Moreover, most weather and climate models use conventional GWs parameterizations, see the review by *Alexander et al.* [2010], in order to describe the interaction with the large-scale flow. In these, GWs are constrained not to travel horizontally. Conventional parameterizations neglect the time-dependence and the horizontal inhomogeneities of the background flow but also the transience of the fields, with potentially important effects [e.g. *Chen et al.*, 2005; *Hasha et al.*, 2008; *Senf and Achatz*, 2011].

The diurnal global-scale variation of the atmosphere is described by STs. These are atmospheric global-scale waves, forced by the periodic heating of solar radiation as described in the work by *Lindzen and Chapman* [1969]. Absorption of solar radiation, large-scale latent-heat release associated with deep convection, and nonlinear dynamics (involving e.g. wave breaking or nonlinear interactions between waves) excite STs [e.g. *Walterscheid and De Vore*, 1981; *Hagan and Forbes*, 2002]. STs consist of a superposition of sub-diurnal oscillations, for example studied by *Forbes and Wu* [2006] and *Zhang et al.* [2006], also because no solar heating is present at night time. Via the modulation of the dynamical

fields, STs influence the propagation of internal GWs [e.g. *Eckermann and Marks*, 1996; *Senf and Achatz*, 2011; *Liu et al.*, 2014b]. The modulation of GW breaking is observed since [*Liu et al.*, 2013]. The effect of horizontal GW propagation and GW transience on the modulation of the GW fields by STs is known to some degree. But we are not aware of any study which addresses the feedback of these effects on the STs themselves. This the focus of the present work.

A detailed description of the GW-ST interaction must incorporate a huge range of spatial scales, from global to sub-meso and below. This is beyond the capacities of present-day computers, while (sub-)mesoscale waves contribute significantly to the wave-mean flow interactions [e.g. *Liu et al.*, 2014a]. Two sets of models were develop in past studies of this interaction. In the first set are linear tidal models, allowing a clear cause-effect relationship, and nonlinear global circulation models [e.g. *Ortland and Alexander*, 2006], where GWs are parameterized quite simply. In the second set, ray-tracing techniques are used to describe GW propagation in a prescribed temporally and spatially varying background flow [e.g. *Eckermann and Marks*, 1996; *Vadas and Fritts*, 2005]. The present study combines these two approaches by coupling a linear tidal model with a GW ray-tracer model.

The ray-tracing scheme is based on *Senf and Achatz* [2011]. A new location-wavenumber phase-space wave-action density conservation scheme has been implemented into this, however, according to *Buhler and McIntyre* [1999b], *Hertzog et al.* [2002] and *Muraschko et al.* [2014]. Each ray can be seen as one of many wave trains constituting together the total GW field. In this spectral approach, however, it is more straightforward to say that it represents a sub-volume of points in location and wavenumber space. Those sub-volumes

propagate in location and wavenumber space along characteristics given by the *Wentzel-Kramers-Brillouin* (WKB) theory. This spectral approach solves (almost completely) classical problems associated with the crossing of rays, see the review about ray-tracer models by *Broutman et al.* [2004]. The wave amplitude of a given spectra element at a given location is predicted from the phase-space wave-action density. In the absence of molecular or nonlinear dissipation the latter is simply conserved along the trajectory of a ray.

The STs are determined using a linear model based on that employed by *Grieger et al.* [2004] and *Achatz et al.* [2008]. It requires as input a climatological mean, including stationary planetary waves, of wind and temperature, here taken from a global circulation model. GW effects are accounted for by spatially varying Rayleigh-friction and Newtonian-relaxation coefficients, see e.g. *Miyahara and Forbes* [1991], *Ortland* [2005] or *McLandress* [2002] for examples of studies using these coefficients. The coupling between ray-tracer and tidal models is done iteratively, similar to the procedure followed by *Meyer* [1999] in the coupling of a tidal model with a Lindzen-Matsuno GW model without horizontal GW propagation and explicit vertical GW propagation: beginning with STs from HAMMONIA, the ray-tracer model is used to determine the diurnally modulated GW fluxes. These are translated into corresponding Rayleigh-friction and Newtonian-relaxation coefficients. The latter are then used in the tidal model to determine new tidal fields. These are used again in the ray-tracer model for the determination of new Rayleigh-friction and Newtonian-relaxation coefficients, and so forth. This is iterated a few times to obtain a converged result on GW depositions and on tidal fields. See the

sketch in Fig. 1. The results are then compared to a *"single-column"* experiment, where the horizontal GW propagation is neglected.

The paper is structured as follows. Next to this introduction (section 1), we give a description of the background flow on which the two sorts of waves propagate (section 2). This is followed by a description of the tidal model (section 3), and then a description of the ray-tracer model (section 4). In section 5, the converged results on GW fluxes and STs are presented, in comparison with the ones from a more conventional parameterization of GWs. A summary is given in section 6.

2. Climatological mean state and solar tides from the HAMMONIA model

The climatological mean fields used both in the tidal model and in the ray-tracer model are taken from the global circulation model HAMMONIA, which is described in detail by *Schmidt et al.* [2006]. The climatological mean includes stationary planetary waves. Monthly averaged values are provided from a twenty years experiment with a spectral truncation at $T48$ and 67 vertical levels using a hybrid pressure coordinate. The data include horizontal wind, temperature and geopotential height. Horizontal wind (U_{BG}, V_{BG}) and temperature T_{BG} are shown in Fig. 2.

The iterative procedure for our study of the GW-ST interaction needs to be initialized. Either one can use in the tidal model a prescribed GW forcing, e.g. by *Wood and Andrews* [1997], or the ray-tracer model can first be used with STs from some other model, e.g. a global circulation model. Both options lead to identical results on the converged GW depositions and ST fields (not shown).

For the second option we have taken STs from the HAMMONIA global circulation model as a reference. They are obtained from monthly mean diurnal cycles (with interval

of 3 hours) from that model. These monthly mean diurnal cycles constitute seasonally dependent STs. The corresponding dynamical fields are decomposed using a time and longitude Fourier transform (Eq. 1).

$$\sum_{n\in\mathbb{N}^*}\sum_{s\in\mathbb{Z}} R_{n,s}\cos(n\Omega_T t + s\lambda) + I_{n,s}\sin(n\Omega_T t + s\lambda) \tag{1}$$

Here t is the time, Ω_T the Earth's rotation rate, λ the longitude, $n(= 1, 2, 3\ldots)$ a sub-harmonic of a solar day and $s(= \ldots -3, -2, -1, 0, 1, 2, 3\ldots)$ the zonal wavenumber. $n = (1, 2, 3)$ represent oscillations with period $(24h, 12h, 8h)$, respectively. These are the diurnal, semi-diurnal and ter-diurnal tides, respectively. Eastward and westward propagation correspond to $(s < 0)$ and $(s > 0)$ respectively. $R_{n,s}$ and $I_{n,s}$ are the cosine part and sine part of the (n, s) tide. $R_{n,s}$ and $I_{n,s}$ can also be called real and imaginary part of a ST. They are latitude-altitude and seasonally dependent.

Here and later, $\|\mathcal{F}\|_{day}$ symbolize the diurnal amplitude of any field $\mathcal{F}$ and $\mathcal{I}m(\mathcal{F})_{day}$ its diurnal sine part.

Tides described with $s = n$ propagate westward at the apparent Sun motion, and are referred to as migrating tides. Absorption of solar radiation by a non-symmetric atmosphere leads to a whole range of east(west)ward ST components. Tides with $s \neq n$ are referred to as non-migrating tides.

For simplicity, the present work is limited to the diurnal $(n = 1)$ ST. Further work will consider semi-diurnal and ter-diurnal tides. In this study, DW_s, respectively DE_s, denote a westward, respectively eastward propagating diurnal tide, s being the absolute value of the zonal wavenumber. D_0 denotes the diurnal standing tide. Some of the important Fourier components of the HAMMONIA diurnal STs are presented later, along

with results from our linear tidal model (see subsection 5.3 and left column of Figs. 7 and 8).

3. Solar-tides model

In our tidal model, the atmosphere is described by a discrete, real, time-dependent, state vector $Y(t)$. This vector comprises the horizontal divergence, vorticity, temperature and surface pressure, all projected on spherical harmonics.

The state vector $Y(t)$ is decomposed into a time-independent mean-state, all tidal components (diurnal, semi-diurnal ...) and the remaining transients. Y_0 denotes the monthly mean reference state vector, Y_n the n-th tide (Y_n^* the corresponding complex conjugate) and $\tilde{Y}(\omega)$ the Fourier transform of the remaining field.

$$\begin{aligned} Y(t) = Y_0 \; + \; & \sum_{n=1}^{\infty} \left(Y_n e^{-in\Omega_T t} + Y_n^* e^{in\Omega_T t} \right) \\ + \; & \int_{\mathbb{R}} \left(\tilde{Y}(\omega) e^{-i\omega t} + \tilde{Y}^*(\omega) e^{i\omega t} \right) \mathrm{d}\omega \end{aligned} \tag{2}$$

STs result from a combination of linear and nonlinear processes. The dynamical equations controlling the state vector $Y(t)$ are decomposed into their linear and nonlinear contributions, respectively named $\mathcal{L}Y$ and $\mathcal{N}[Y]$, to which is added a forcing or heating component $\mathcal{F}[Y]$. The forcing or heating $\mathcal{F}[Y]$ includes e.g. the solar absorption and the GW drag. The nonlinear part $\mathcal{N}[Y]$ of the dynamical system includes quadratic and non-quadratic terms, e.g. from the advective derivatives. The linear term $\mathcal{L}Y$ includes, e.g., the Coriolis contribution.

$$\partial_t Y(t) = \mathcal{L}Y + \mathcal{N}[Y] + \mathcal{F}[Y] \tag{3}$$

Our linear tidal model is in many aspects identical to the linear model used by *Grieger et al.* [2004] and *Achatz et al.* [2008]. The model has been obtained by linearizing the primitive equation code KMCM (Kühlungsborn Mechanistic Circulation Model, details on the model by *Becker and Schmitz* [2003]), in its conservative-adiabatic version, about some arbitrary reference state Y_0. This has been done using the automatic differentiation tool TAMC (Tangent Adjoint Model Compiler) developed by *Giering and Kaminski* [1998], and resulting in $\mathcal{L}_0 Y$ for any input Y. $\mathcal{L}_0 Y$ includes the linear term $\mathcal{L}Y$ but also the linearization of $\mathcal{N}[Y]$ about Y_0. The linear model uses the HAMMONIA climatological mean as reference state Y_0 (see section 2). The forcing of the tidal model includes the diurnal cycle of the heating rates in HAMMONIA data, denoted here $\mathcal{Q}_1$ and discussed by *Achatz et al.* [2008].

Neglected nonlinearities are taken into account by linear parameterization. To prevent any problem in the integration process, we add a molecular thermal conductivity as in *Vial* [1986]. This represents a small dissipative process which rises as density decreases, also used in *Wood and Andrews* [1997]. No additional dissipative processes are included.

GW dynamics is coupled iteratively to the STs (Fig. 1). The propagation and saturation / breaking (in our ray-tracer model) of GWs leads to a deposition of momentum and entropy. The deposition is projected onto the ST fields and their tendencies. From the projections, Rayleigh-friction and Newtonian-relaxation coefficients $(\gamma^{\mathcal{R}}, \gamma^{\mathcal{I}})$ are calculated, as described later in details (see section 4). Rayleigh-friction and Newtonian-relaxation coefficients are latitude, altitude and seasonally dependent. They form an approximate diurnal forcing, due to GWs, of diurnal STs, and given by Eq. 4.

$$-\gamma^{\mathcal{R}} Y_1 - \frac{\gamma^{\mathcal{I}}}{\Omega_T} \partial_t Y_1 \tag{4}$$

197 Adding the different contributions, the linear tidal model leads to Eq. 5 for the diurnal
198 ST state vector Y_1. Positives (negatives) values of the Rayleigh-friction and Newtonian-
199 relaxation coefficients $\gamma^{\mathcal{R}}$ are thus associated with a deceleration (acceleration) of the
200 diurnal tides and imaginary coefficients $\gamma^{\mathcal{I}}$ influence the diurnal ST phases (Eq. 5).

$$\Big(1 + \frac{\gamma^{\mathcal{I}}}{\Omega_T}\Big) \partial_t Y_1 \;=\; \Big(\mathcal{L}_0 - \gamma^{\mathcal{R}}\Big) Y_1 + \mathcal{Q}_1 \tag{5}$$

201 Our linear tidal model has a spectral truncation at $T48$ and uses 67 vertical levels.
202 The overall linear operator on Eq. 5 is dimensionally too big for direct matrix inversion.
203 Instead we integrate Eq. 5 using a fourth order Runge-Kutta scheme with a fixed time
204 step of $\Delta t = 120\,s$ (convergence checked), but a forcing $\mathcal{Q}_1$ gradually increasing from
205 $(t = 0)$ to $(t = 1\,day)$. The model is integrated in total over $20\,days$. The last $5\,days$ are
206 used for a determination of the diurnal ST by Fourier analysis.

4. Gravity-wave model

207 Our ray-tracer model describes the linear evolution of GW trains propagating in a three-
208 dimensional global-scale time-changing flow. It computes GW propagation, refraction and
209 dissipation through a prescribed arbitrary atmosphere (time and spatially dependent)
210 under the WKB approximation. This is the natural setting for unresolved, sub-grid-scale
211 waves. The background flow includes a climatological mean (section 2) and diurnal STs
212 (section 3).

The model is based on the work by *Senf and Achatz* [2011]. It has been modified by the implementation of a new phase-space wave-action density scheme (subsections 4.3 and 4.6), according to *Buhler and McIntyre* [1999b], *Hertzog et al.* [2002] and *Muraschko et al.* [2014], as detailed below.

4.1. Global ray-tracer model

GWs are assumed, in our model, to be described by the real part of a complex field, with a slowly varying amplitude and a rapidly varying small-scale wave-phase $\phi(\mathbf{x}, t)$. The phase derivatives define the slowly varying wavenumber vector $\mathbf{k} = \nabla_{\mathbf{x}}\phi = k\mathbf{e}_\lambda + l\mathbf{e}_\theta + m\mathbf{e}_\mathbf{r}$ and the slowly varying absolute frequency $\omega = -\partial_t\phi$. $\mathbf{e}_\lambda$, $\mathbf{e}_\theta$ and $\mathbf{e}_\mathbf{r}$ are the usual zonal, meridional and radial unit vector. $\nabla_\mathbf{x} = \mathbf{e}_\lambda/[r\cos(\theta)]\partial_\lambda + \mathbf{e}_\theta/r\partial_\theta + \mathbf{e}_\mathbf{r}\partial_r$ denotes the spherical gradient and $\nabla_\mathbf{k}$ the wavenumber gradient.

A local dispersion relation and polarization relations between GW amplitudes are obtained to leading order of the scale-separation parameter. Our model uses the dispersion relation (Eq. 6) of GWs in a rotating stratified atmosphere under Boussinesq approximation, valid for waves with vertical scale less than the atmospheric scale height. Our model also uses the corresponding polarization relations.

$$\begin{aligned} \Omega(\mathbf{x}, \mathbf{k}, t) &= \omega \\ &= \mathbf{k} \,.\, \mathbf{U} + \hat{\omega} \\ &= \mathbf{k} \,.\, \mathbf{U} \pm \sqrt{\frac{N^2(k^2 + l^2) + f^2 m^2}{k^2 + l^2 + m^2}} \end{aligned} \tag{6}$$

The spatially-dependent background flow evolves in time due here to STs. $N(\mathbf{x}, t)$ is the reference buoyancy frequency, $f(\theta)$ the local latitude-dependent Coriolis parameter, $\mathbf{U}(\mathbf{x}, t) = U\mathbf{e}_\lambda + V\mathbf{e}_\theta$ the horizontal background wind and $\hat{\omega}$ denotes the intrinsic frequency. If $\hat{\omega} > 0$, GWs with upward propagating group velocity are associated with $m < 0$, $k > 0$

denotes waves with positive zonal intrinsic group velocity and $l > 0$ northward intrinsic group velocity (see group velocities in Eq. 9).

GW trains propagate along characteristics given by Eq. 7 and Eq. 8.

$$d_t \mathbf{x} = \mathbf{c_g} \tag{7}$$
$$d_t \mathbf{k} = -\nabla_{\mathbf{x}} \Omega \tag{8}$$

$d_t = \partial_t + \mathbf{c_g} \cdot \nabla_{\mathbf{x}}$ is the time derivative along a ray. $\mathbf{c_g} = \nabla_{\mathbf{k}} \Omega = c_{g\lambda} \mathbf{e}_\lambda + c_{g\theta} \mathbf{e}_\theta + c_{gz} \mathbf{e_r}$ denotes the absolute group velocity and $\hat{\mathbf{c}}_\mathbf{g} = \mathbf{c_g} - \mathbf{U}$ the intrinsic group velocity. The geometric position $\mathbf{x}$, the wavenumber vector $\mathbf{k}$ and the absolute frequency ω evolve during the propagation. Projecting Eqs. 7 and 8 on spherical coordinates leads to the governing equations of propagation (Eq. 9) of our global three-dimensional ray-tracer model, with standard norm $\|\mathbf{k}\|^2 = k^2 + l^2 + m^2$. Details of the calculation are given in *Hasha et al.* [2008].

The ray-tracer model integrates Eq. 9 along each ray-path. Modifications observed in GWs characteristics are induced by background flow (spatial and temporal) changes along the propagation. The implementation is described in subsection 4.3 where the use of the additional and redundant ω-equation is discussed as well.

$$
\left\{
\begin{array}{rcccl}
d_t\lambda &=& \dfrac{c_{g\lambda}}{r\cos(\theta)} &=& \dfrac{1}{r\cos(\theta)}\Big(U + \dfrac{k}{\hat{\omega}\|\mathbf{k}\|^2}(N^2-\hat{\omega}^2)\Big) \\
d_t\theta &=& \dfrac{c_{g\theta}}{r} &=& \dfrac{1}{r}\Big(V + \dfrac{l}{\hat{\omega}\|\mathbf{k}\|^2}(N^2-\hat{\omega}^2)\Big) \\
d_t r &=& c_{gr} &=& -\dfrac{m}{\hat{\omega}\|\mathbf{k}\|^2}\,(\hat{\omega}^2-f^2) \\
d_t\omega &=& \mathbf{k}\,.\,\partial_t\mathbf{U} &+& \dfrac{k^2+l^2}{2\hat{\omega}\|\mathbf{k}\|^2}\,\partial_t N^2 \\
d_t k &=& -\dfrac{\mathbf{k}\,.\,\partial_\lambda\mathbf{U}}{r\cos(\theta)} &-& \dfrac{k^2+l^2}{2\hat{\omega}\|\mathbf{k}\|^2 r\cos(\theta)}\,\partial_\lambda N^2 \\
&&&+& \dfrac{c_{g\lambda}}{r}\Big(l\tan(\theta)-m\Big) \\
d_t l &=& -\dfrac{\mathbf{k}\,.\,\partial_\theta\mathbf{U}}{r} &-& \dfrac{k^2+l^2}{2\hat{\omega}\|\mathbf{k}\|^2 r}\,\partial_\theta N^2 - \dfrac{m^2}{2\hat{\omega}\|\mathbf{k}\|^2 r}\,\partial_\theta f^2 \\
&&&-& \dfrac{1}{r}\Big(k\tan(\theta)c_{g\lambda} + m c_{g\theta}\Big) \\
d_t m &=& -\mathbf{k}\,.\,\partial_r\mathbf{U} &-& \dfrac{k^2+l^2}{2\hat{\omega}\|\mathbf{k}\|^2}\,\partial_r N^2 \\
&&&+& \dfrac{1}{r}\Big(k c_{g\lambda} + l c_{g\theta}\Big)
\end{array}
\right. \tag{9}
$$

Eq. 9 describes the effect of spatial and temporal background variations on the GWs. The wavenumber norm $\|\mathbf{k}\|^2$ only evolves due to background flow changes along the propagation. Curvature terms do not change the wavenumber norm $\|\mathbf{k}\|^2$, but tilt the wavenumber direction $\mathbf{k}/\|\mathbf{k}\|$. Note that this is not the case in the ray-tracer equations, projected in spherical coordinates, as written in *Hasha et al.* [2008], so that we have modified them accordingly.

Conventional GW parameterizations neglect horizontal wavenumber changes due to background flow horizontal gradients. Conventional GW parameterizations also neglect horizontal wave propagation. In a scheme under this *"single-column"* approximation, $\Omega(\mathbf{x},\mathbf{k},t)$ is assumed formally independent of (λ,θ), and (k,l) are both constant along rays. For consistency, the curvature terms are as well ignored in such approximation. For simulations in *"single-column"* approximation, we impose :

$$d_t\lambda = d_t\theta = d_tk = d_tl = 0 \tag{10}$$

The time dependence of the background flow, due here to diurnal STs, causes a modulation of the GW frequency ω along the propagation, as expressed by the ω equation and as was studied e.g. by *Eckermann and Marks* [1996].

Eq. 9 gives the position and the time evolution of all intrinsic GW characteristics but its amplitude. In the absence of forcing and dissipation, the ray amplitude is governed by (Eq. 11) the conservation of the wave-action density $A = E/\hat{\omega}$, E being the disturbance energy density per unit of volume, following e.g. *Bretherton and Garrett* [1968] and *Grimshaw* [1975].

$$\partial_t A + \nabla_{\mathbf{x}\cdot}(A\mathbf{c_g}) = d_tA + A\nabla_{\mathbf{x}} \cdot \mathbf{c_g} = 0 \tag{11}$$

The divergence of the group velocity determines the evolution of the wave-action density. As described later, see subsection 4.6, our ray-tracer model does not use Eq. 11 directly. Following *Buhler and McIntyre* [1999b], *Hertzog et al.* [2002] and *Muraschko et al.* [2014], it rather uses phase-space wave-action density, thereby avoiding problems associated with the crossing of rays, namely caustics.

4.2. Gravity wave source

GW sources include several aspects in addition to topography (see the review by *Fritts and Alexander* [2003] and e.g. *de la Camara et al.* [2014]), a non-exhaustive list containing wind shear [e.g. *Buhler and McIntyre*, 1999a], convection [e.g. *Song and Chun*, 2005; *Choi and Chun*, 2011], fronts and jets [e.g. *de la Camara and Lott*, 2015]. The inclusion of

corresponding sources into our GW model is left to future work. Here, however, we use for simplicity a small highly idealized GW ensemble, listed in Table 1.

This follows the work by *Becker and Schmitz* [2003] who have shown that the mean residual circulation of middle-atmosphere is well reproduced in a global circulation model with a small GW ensemble, using a single-column *Lindzen* parameterization. *Meyer* [1999] also uses a small idealized GW ensemble in a study of the GW-ST interaction.

The GW ensemble from *Becker and Schmitz* [2003] is used in this study, as it was by *Senf and Achatz* [2011]. A horizontally homogeneous lower-boundary condition is assumed for the ray-tracer model, where GWs are emitted homogeneously at a lower-boundary, $\hat{z}_B = 25\,km$ ($\hat{z}$ denotes the average geopotential height of a hybrid model level, see subsection 4.3), in different azimuthal directions. GWs have initial horizontal phase velocities $6.8\,m/s \leq c_H \leq 30\,m/s$, horizontal wavelengths $380\,km \leq L_H \leq 600\,km$ and vertical fluxes of horizontal momentum $0.2\,kg/m/s/day \leq F_H \leq 0.4\,kg/m/s/day$. The GW ensemble is non-isotropic with smaller horizontal wavenumber $\mathbf{k_H}$, larger horizontal absolute phase velocities c_H and larger vertical flux of horizontal momentum F_H pointing westward. The non-isotropy of the GW source has been introduced by *Becker and Schmitz* [2003] to obtain a realistic horizontal wind climatology with their general circulation model. In comparison with *Senf and Achatz* [2011] study, flux of horizontal momentum are a factor 100 smaller at equivalent launch level. This factor has been chosen so as to obtain magnitudes in GW depositions roughly corresponding to what one expects for the closure of the mesospheric jets.

The background fields (climatological mean plus STs) are given on a global (λ, θ, r) grid. Rays are initialized at the launch location $\hat{z}_B = 25\,km$ by specifying horizontal wavenum-

ber k_H and horizontal phase velocity c_H magnitude and direction (Table 1). Intrinsic frequency $\hat{\omega}$ and vertical wavenumber m are computed using the dispersion relation (Eq. 6), imposing an upward direction of the initial local group velocity. The local wave-action density $A = E/\hat{\omega}$ is obtained from the initial vertical flux of horizontal momentum F_H using the polarization relations (see subsection 4.5 below). Each ray of each GW ensemble member is integrated forward separately.

Each ray characterizes a finite-volume in position-wavenumber phase-space. Specific details on that volume are given below, in subsection 4.6. One ray, or phase-space finite-volume, is emitted initially per grid cell on the horizontal (λ, θ) grid at the lower-boundary at $\hat{z}_B = 25\,km$. New rays are emitted in the course of a simulation if a ray volume has propagated vertically by more than its original vertical extent (Fig. 3). We found this approach more consistent with our position-wavenumber scheme, as it ensures a fixed lower boundary condition for the GW fields. In contrast to this, *Senf and Achatz* [2011] have launched new rays at every time step. The implementation of more realistic GW sources is left to future work.

4.3. Numerical implementation

Since the background fields are defined on a pre-defined spatial grid, while the rays move freely in space, so background fields must be interpolated to the ray positions for use in the ray equations, while the momentum and buoyancy fluxes due to the ray must be mapped onto the grid, so as to obtain an output of use for the tidal model. The background fields are interpolated to the ray location via a linear polygonal interpolation.

A further complication is that the grid of the tidal model uses hybrid vertical levels with time and spatially dependent vertical position. Here each hybrid level is characterized by

its horizontal-mean geopotential height. For the direct applicability of background flow data, it is therefore necessary to identify the horizontal-mean geopotential height ($\tilde{z}$, hybrid coordinate) of the vertical position of a ray. If $\mathbf{c_{gH}}$ denotes the horizontal group velocity vector, each change of altitude r along the ray can be expressed by Eq. 12, leading to a governing equation for the evolution of the corresponding hybrid-level coordinate (Eq. 13).

$$d_t r = \partial_t r + (d_t \lambda)\partial_\lambda r + (d_t \theta)\partial_\theta r + (d_t \tilde{z})\partial_{\tilde{z}} r \tag{12}$$

$$d_t \tilde{z} = \frac{1}{\partial_{\tilde{z}} r}\Big(c_{gz} - \partial_t r - \mathbf{c_{gH}} \cdot \nabla_{\mathbf{x}} r\Big) \tag{13}$$

The time-integration of the ray equations (Eq. 9 plus wave-action density in position-wavenumber phase-space) is done in two stages. First, an integration estimate is obtained from a Runge-Kutta third order scheme with a fixed time step of $\Delta t = 300\,s$. Second, an optimization technique is used to adaptively change all ray properties until the dispersion relation is retained (details by *Senf and Achatz* [2011]). The two-stage scheme assumes that wavenumber $\mathbf{k}$ and frequency ω both evolve. The redundant information gained by the ω-equation in (Eq. 9) is therefore used to correct numerical errors and stabilize the implemented method.

Convergence of our results has been checked with regard the length of the employed time step, and the integration period (not shown). Presented results are averaged over $2\,days$. No explicit WKB validity test is performed. Only rays which cross the extreme thresholds of $100\,km$ vertical wavelength or $10\,days$ intrinsic period are removed. Similar results are found with different threshold (not shown). As noted by *Sartelet* [2003], ray theory performs remarkably well even if the scale separation assumption is not fulfilled.

4.4. Wave saturation

Wave saturation schemes are heuristic methods by which nonlinear wave breaking can be modeled within a linear ray-tracer model. Numerous saturation schemes exist and we choose, for reasons of simplicity, static stability as criteria for the GW breaking of a monochromatic wavepacket. This will be improved in future work.

(u', v', w') denote the zonal, meridional and vertical GW velocity components. b' denotes the GW buoyancy and ρ the background flow density. From the polarization relations associated with the GW dispersion relation (Eq. 6), the energy disturbance density E is given by Eq. 14, where an extra factor 1/2 results from the phase averaging, and (u', v', w', b') denote respective amplitudes.

$$\begin{aligned} E &= \frac{\rho}{2}\Big(\frac{|u'|^2}{2} + \frac{|v'|^2}{2} + \frac{|w'|^2}{2} + \frac{|b'|^2}{2N^2}\Big) \\ &= \frac{\rho}{2}\Big(1 + \frac{f^2 m^2}{N^2(k^2+l^2)}\Big)\frac{|b'|^2}{N^2} \\ &= \frac{\rho}{2}\Big(1 + \frac{m^2}{k^2+l^2}\Big)\hat{\omega}^2\frac{|b'|^2}{N^4} \end{aligned} \tag{14}$$

According to the static-stability criterion a GW breaks if its vertical buoyancy gradient is sufficiently large to neutralize or overturn the ambient potential-temperature gradient. At the breaking threshold, the GW buoyancy amplitude b' and the buoyancy frequency N therefore satisfy the relation $N^2 = |b'm|$. This relation can be converted into a saturation threshold A_{Sat} for the wave-action density $A = E/\hat{\omega}$ (Eq. 15).

$$A_{Sat} = \frac{\rho}{2}\Big(1 + \frac{m^2}{k^2+l^2}\Big)\frac{\hat{\omega}}{m^2} \tag{15}$$

There is no dissipation if $A < A_{Sat}$. As density decreases with altitude, however, GWs ultimately break, the wave action is reduced to its threshold value.

The saturation scheme is applied to each ray separately, before momentum and buoyancy GW fluxes due to the ray, are mapped onto the background pre-defined spatial grid, this last part being explained in the next two sub-sections.

4.5. Momentum and buoyancy deposition

GW-mean-flow interaction is mediated by a deposition of momentum and buoyancy. In addition to define the energy disturbance density E (Eq. 14), the polarization relations also help us to determine the momentum and buoyancy fluxes needed in the calculation of the various depositions. The obtained expressions are listed below (Eq. 16). Note that the vertical flux of horizontal momentum F_H, used in the GW ensemble (see Table 1), equals $\|\rho \mathbf{u'_H} w'\|$, where $\mathbf{u'_H}$ is the horizontal GW velocity.

$$\begin{cases} \rho u'^2 \equiv A\hat{c}_{g\lambda} k \left(1 - \dfrac{1+(l/k)^2}{1-(\hat{\omega}/f)^2}\right) \\ \rho u'v' \equiv A\hat{c}_{g\theta} k \\ \rho v'^2 \equiv A\hat{c}_{g\theta} l \left(1 - \dfrac{1+(k/l)^2}{1-(\hat{\omega}/f)^2}\right) \\ \rho \mathbf{u'_H} w' \equiv A\hat{c}_{gr} \dfrac{\mathbf{k_H}}{1-(f/\hat{\omega})^2} \\ \rho w'^2 \equiv A\hat{\omega} \dfrac{k^2+l^2}{\|\mathbf{k}\|^2} \\ \rho w'b' \equiv 0 \\ \rho \mathbf{u'_H} b' \equiv A \dfrac{mfN^2}{\hat{\omega}\|\mathbf{k}\|^2}(\mathbf{k_H} \times \mathbf{e_r}) \end{cases} \tag{16}$$

Note that momentum horizontal fluxes $\rho \mathbf{u'_H} w'$ are linked to the horizontal buoyancy fluxes $\rho \mathbf{u'_H} b'$ (Eq. 17), as follows from Eq. 16.

$$f\mathbf{e_r} \times \rho \mathbf{u'_H} w' = \left(\frac{\hat{\omega}}{N}\right)^2 \rho \mathbf{u'_H} b' \tag{17}$$

Our ray-tracer model calculates the various fluxes on the global (λ, θ, r) grid. Fluxes corresponding to a ray volume (Eq. 16) are only deposited at its location in position-

space. Adding the contribution of all the rays, and using a distance-weighted filtering procedure, gives the total value of the various fluxes (Eq. 16) on the global pre-defined (λ, θ, r) grid.

The convergence of momentum and buoyancy fluxes is then obtained in spherical coordinate (Eq. 18). Following *Senf and Achatz* [2011], f_x (f_y) denotes the zonal (meridional) GW convergence of momentum flux and f_b the GW convergence of buoyancy. Positive (negative) values of $f_{x,y,b}$ are therefore associated with an acceleration (deceleration) of the surrounding flow, either for the climatological mean or for the STs.

$$\begin{cases} f_x \equiv -\dfrac{1}{\rho}\nabla_{\mathbf{x}} \cdot (\rho \mathbf{v}' u') \\ f_y \equiv -\dfrac{1}{\rho}\nabla_{\mathbf{x}} \cdot (\rho \mathbf{v}' v') \\ f_b \equiv -\dfrac{1}{\rho}\nabla_{\mathbf{x}} \cdot (\rho \mathbf{v}' b') \end{cases} \tag{18}$$

The GW forcing of the climatological mean flow is given by the daily mean of GW flux-convergences $f_{x,y,b}$. The forcing of diurnal STs is given by the diurnal modulation of these flux-convergences $f_{x,y,b}$.

GW effects on climatological mean and STs (as needed in the tidal model) can be quantified using Rayleigh-friction and Newtonian-relaxation coefficients and have already been used in the context of GW-ST interaction [e.g. *Miyahara and Forbes*, 1991; *Ortland*, 2005; *McLandress*, 2002]. These coefficients measure the zonally averaged projection of the convergence-fluxes $f_{x,y,b}$ onto the diurnal tidal components and tendencies. They are given by Eq. 19.

$$\begin{cases} \gamma_x^{\mathcal{R}} \equiv -\dfrac{< U_{ST} f_x >}{< U_{ST}^2 >} & , \quad \gamma_x^{\mathcal{I}} \equiv -\Omega_T \dfrac{< \partial_t U_{ST} f_x >}{< (\partial_t U_{ST})^2 >} \ , \\ \gamma_y^{\mathcal{R}} \equiv -\dfrac{< V_{ST} f_y >}{< V_{ST}^2 >} & , \quad \gamma_y^{\mathcal{I}} \equiv -\Omega_T \dfrac{< \partial_t V_{ST} f_y >}{< (\partial_t V_{ST})^2 >} \ , \\ \gamma_b^{\mathcal{R}} \equiv -\dfrac{< B_{ST} f_b >}{< B_{ST}^2 >} & , \quad \gamma_b^{\mathcal{I}} \equiv -\Omega_T \dfrac{< \partial_t B_{ST} f_b >}{< (\partial_t B_{ST})^2 >} \ . \end{cases} \tag{19}$$

We denote here by (U_{ST}, V_{ST}, B_{ST}) the zonal, meridional and buoyancy diurnal tidal fields. $\gamma_{x,y,b}^{\mathcal{R}}$ denotes the different projections of the GW flux-convergences (Eq. 18) onto diurnal tidal fields. Projections onto their tendencies are denoted by $\gamma_{x,y,b}^{\mathcal{I}}$. $< \ldots >$ represents a zonal and temporal average. Rayleigh-friction and Newtonian-relaxation coefficients depend on latitude, altitude, and the season. These coefficients are used in our linear tidal model (see section 3) to capture the impact of GW dynamics on STs.

Conventional GW parameterizations in linear tidal models often prescribe $\gamma_{x,y,b}^{\mathcal{I}} = 0$ while $\gamma_{x,y,b}^{\mathcal{R}}$ is positive and only depends on altitude. This kind of GW parameterization was for example used in *Wood and Andrews* [1997]. It thus accounts for a standard dissipative process. In the GW breaking zone, $\gamma_{x,y,b}^{\mathcal{R}}$ roughly equals $1\, day^{-1}$.

We now explain why these coefficients need to be rescaled. For a given zonal wavenumber s, $f_x^{\mathcal{R}}(s)$ and $f_x^{\mathcal{I}}(s)$ respectively denote the cosine and sine part of the flux convergence f_x. Its diurnal part is named f_x^{day}. U_{ST}, $U_{ST}^{\mathcal{R}}(s)$ and $U_{ST}^{\mathcal{I}}(s)$ are defined likewise. The diurnal forcing f_x^{day} due to the GWs (Eq. 20) is approximated by Eq. 21.

$$f_x^{day} = \sum_{s \in \mathbb{Z}} f_x^{\mathcal{R}}(s) \cos(\Omega_T t + s\lambda) + f_x^{\mathcal{I}}(s) \sin(\Omega_T t + s\lambda) \tag{20}$$

$$\approx -\gamma_x^{\mathcal{R}} U_{ST} - \frac{\gamma_x^{\mathcal{I}}}{\Omega_T} \partial_t U_{ST} \tag{21}$$

The projections of f_x on U_{ST} and $\partial_t U_{ST}/\Omega_T$ are shown in Eqs. 22 and 23. Because GW depositions are modulated by more than one unique STs zonal component, $\sqrt{< U_{ST}\, f_x >^2 \, + \, < \partial_t U_{ST}/\Omega_T \, f_x >^2}$ will not equals $\sqrt{< |U_{ST}|^2 >< |f_x^{day}|^2 >}$, even if it

was expected due to the approximation. For that purpose we rescaled $\gamma^{\mathcal{R},\mathcal{I}}_{x,y,b}$ so that Eq. 24 is fulfilled (and equivalently for V_{ST} and B_{ST}).

$$< U_{ST} f_x > = \sum_{s\in\mathbb{Z}} f^{\mathcal{R}}_x(s) U^{\mathcal{R}}_{ST}(s) + f^{\mathcal{I}}_x(s) U^{\mathcal{I}}_{ST}(s) \tag{22}$$

$$< \partial_t U_{ST}/\Omega_T f_x > = -\sum_{s\in\mathbb{Z}} f^{\mathcal{R}}_x(s) U^{\mathcal{I}}_{ST}(s) - f^{\mathcal{I}}_x(s) U^{\mathcal{R}}_{ST}(s) \tag{23}$$

$$\int_0^{+\infty}\int_{-\frac{\pi}{2}}^{\frac{\pi}{2}} \mathrm{d}z\mathrm{d}\theta < |f^{day}_x|^2 > = \int_0^{+\infty}\int_{-\frac{\pi}{2}}^{\frac{\pi}{2}} \mathrm{d}z\mathrm{d}\theta \Big(|\gamma^{\mathcal{R}}_x|^2 + |\gamma^{\mathcal{I}}_x|^2 \Big) < |U_{ST}|^2 > \tag{24}$$

At last, to prevent any problems in the integration of the linear tidal model (section 3), we remove negative values of $\gamma^{\mathcal{R}}_{x,y,b}$ in the thermosphere (hybrid levels higher than $130\,km$ and up to the top at $300\,km$), as HAMMONIA global circulation model, as ours, were not meant to study the high atmosphere. Corresponding removed coefficients satisfy $1/\gamma^{\mathcal{R}}_{x,y,b} \geq -4\,day$. Similar results for the middle-atmosphere are found with different threshold (not shown).

4.6. Wave-action phase-space density conservation

Ray-tracer models associate a position $\mathbf{x}$ with a single wavenumber $\mathbf{k}$. Caustics arise when two rays with different wavenumbers coincide, see the review paper about ray-tracer models from *Broutman et al.* [2004] for more details. Caustics thus represent an apparent breakdown of the basic assumptions of WKB theory. Moreover, they can lead to stability problems in the numerical simulation of GW mean-flow interactions, as studied by *Rieper et al.* [2013] and *Muraschko et al.* [2014]. However, as shown by *Muraschko et al.* [2014], most caustic problems disappear in the formalism of *Buhler and McIntyre* [1999b] and *Hertzog et al.* [2002], where the conservation of wave-action density (Eq. 11) is recast as a transport equation in position-wavenumber phase-space. This approach is adopted in the present study.

As the basic WKB theory is linear, direct GW-GW interaction are not captured and the spectral approach here adopted does not change that point.

The derivation follows *Muraschko et al.* [2014] and so is not reproduced here. δ is the Dirac delta function and $\mathcal{N}$ denotes the phase-space wave-action density, defined by Eq. 25, using the wave-action density $A(\mathbf{x},t)$. A superposition of (possible infinitely) many wave-trains is considered for the definition, each of them being defined by a finite-volume in position-wavenumber phase-space $\mathcal{V}_\alpha(\mathbf{x}_\alpha,\mathbf{k}_\alpha,t)=d^3xd^3k$, centered on a position $\mathbf{x}_\alpha$ and a wavenumber $\mathbf{k}_\alpha$, and by a wave-action density $A_\alpha(\mathbf{x},t)$. The sub-volume in wavenumber-space of the finite-volume $\mathcal{V}_\alpha(\mathbf{x}_\alpha,\mathbf{k}_\alpha,t)$ is denoted $\mathcal{V}_\alpha^{\mathbf{k}}(t)$. The ensemble $\mathbb{E}$ includes all the vector pointers α, each of them is meant to define a ray.

$$A(\mathbf{x},t)=\sum_{\alpha\in\mathbb{E}}A_\alpha(\mathbf{x},t)=\sum_{\alpha\in\mathbb{E}}\int_{\mathbf{k}\in\mathcal{V}_\alpha^{\mathbf{k}}(t)}\mathcal{N}(\mathbf{x},\mathbf{k},t)\mathrm{d}\mathbf{k} \tag{25}$$

Note that classic wave-action density is simply the integral of phase-space wave-action-density in wavenumber-space. The derivation ultimately leads to Eq. 26, using Eqs. 7, 8 and 11 in the calculation. Eq. 26 describes the transport of phase-space wave-action density $\mathcal{N}$ in position-wavenumber phase-space.

$$0=\partial_t\mathcal{N}+\nabla_{\mathbf{x}}\centerdot(\mathbf{c_g}\mathcal{N})+\nabla_{\mathbf{k}}\centerdot(d_t\mathbf{k}\mathcal{N}) \tag{26}$$
$$0=\nabla_{\mathbf{x}}\centerdot\mathbf{c_g}+\nabla_{\mathbf{k}}\centerdot d_t\mathbf{k} \tag{27}$$

By definition ($\mathbf{c_g}=\nabla_{\mathbf{k}}\Omega, d_t\mathbf{k}=-\nabla_{\mathbf{x}}\Omega$), the position-wavenumber phase-space group velocity is divergence free (Eq. 27) and rays so are associated with a preserved volume in position-wavenumber phase-space (Eq. 27). The position-wavenumber volume $\mathcal{V}_\alpha(\mathbf{x}_\alpha,\mathbf{k}_\alpha,t)$ is conserved during the propagation, responding in shape to the local stretching and squeezing in position-wavenumber phase-space.

Because of Eqs. 26 and 27, the phase-space wave-action density $\mathcal{N}$ is conserved along characteristics in position-wavenumber phase-space (Eq. 28). Eq. 28 contrasts with the wave-action density conservation (Eq. 11), in which formalism wave-action density is not conserved along the propagation. The initial distribution of phase-space wave-action density $\mathcal{N}(\mathbf{x}, \mathbf{k}, t = 0)$, advected conservatively along position-wavenumber phase-space trajectories, gives the distribution at any time $t > 0$.

$$0 = \partial_t \mathcal{N} + \mathbf{c_g} \cdot \nabla_{\mathbf{x}} \mathcal{N} + d_t \mathbf{k} \cdot \nabla_{\mathbf{k}} \mathcal{N} \tag{28}$$

In the numerical implementation, the phase-space wave-action density $\mathcal{N}(\mathbf{x}, \mathbf{k}, t)$ is assumed to be uniform within one ray volume. Eq. 25 leads then to a simple conversion process from $\mathcal{N}(\mathbf{x}, \mathbf{k}, t)$ to the wave-action density $A_\varsigma(\mathbf{x}, t)$ ray-contribution, given by Eq. 29.

$$A_\varsigma(\mathbf{x}, t) = \mathcal{N}(\mathbf{x}, \mathbf{k}_\varsigma, t) \times \mathcal{V}_\varsigma^{\mathbf{k}}(t) \tag{29}$$

In the numerical implementation, phase-space is subdivided into finite-volumes comprising many spectral components (see table 1). These finite-volumes $\mathcal{V}_\varsigma(\mathbf{x}_\varsigma, \mathbf{k}_\varsigma, t)$ evolve in phase-space according to the ray equations (Eq. 9), possibly being strongly deformed. We stress that in the present implementation the saturation criterion is applied to each $A_\varsigma(\mathbf{x}, t)$ separately. A better approach is planned for the future, where the superposition of all rays at a given spatial location is taken into account.

The initial finite-volume in position-space corresponds to the local grid-cell size in the global background pre-defined grid and is thus different from one location to an other. In

458 the present work, the wavenumber-space finite-volume $\mathcal{V}_{\varsigma}^{\mathbf{k}}(t)$ equals $\Delta k \times \Delta l \times \Delta m$ and is
459 taken to be the same (initially) for all ray volumes. Initial values of the zonal-wavenumber
460 Δk, the meridional-wavenumber Δl and the vertical-wavenumber Δm correspond to typi-
461 cal wavenumber differences between the different GW ensemble members (Table 1). Initial
462 values are $1/\Delta k = 1/\Delta l = 310\,km$ and $1/\Delta m = 3.1\,km$.

463 The initial finite-volume of each ray in location-wavenumber phase-space is a
464 rectangular-box. For simplicity it is assumed to remain a rectangular-box along ray prop-
465 agation (Fig. 3). This approximation was found to be successful by *Muraschko et al.*
466 [2014]. Therefore, during the propagation, only side lengths of the rectangle have to be
467 predicted.

468 Neglecting the contribution of the curvature terms (Eq. 9), the six equations governing
469 the local position-wavenumber phase-space stretching and squeezing of the finite-volume
470 are reduced to only three.

471 That simplification is due to the two-by-two volume conservation laws obtained because
472 of the "no-curvature contribution" approximation ; e.g. in the altitude-vertical wavenum-
473 ber plane $\partial_r c_{gr} + \partial_m d_t m = 0$. The vertical-length $\Delta r(t)$ times the vertical-wavenumber
474 dimension $\Delta m(t)$ of the finite volume is therefore a preserved quantity along the ray propa-
475 gation : $\Delta r(t)\Delta m(t) = \Delta r(t=0)\Delta m(t=0)$. A squeezing in altitude $\Delta r(t) < \Delta r(t=0)$
476 is thus associated with a stretching in vertical wavenumber $\Delta m(t) > \Delta m(t=0)$ and
477 vice versa. The finite-volume evolution in wavenumber-space is then given by relations
478 such as : $\Delta m(t) = \Delta r(t=0)\Delta m(t=0)/\Delta r(t)$. Only aspect ratios change during the
479 propagation. Equivalent relations also exist for the other four directions (λ, θ, k, l).

No explicit WKB validity test is performed. Only rays which cross the extreme threshold of being squeezed or stretched by a factor 20 in one direction are removed (e.g. $\Delta r(t) > 20\Delta r(t=0)$ or $\Delta r(t) < \Delta r(t=0)/20$). The value of this threshold is not found to affect our results significantly (not shown).

With regard to the lower-boundary condition (source) described in subsection 4.2, it was found that similar results are obtained with a higher density of emission (for example two rays per grid-cell) but weaker associate finite-volume in position-space (not shown). We also checked that modifying the initial area $V_\varsigma(t=0)$ in wavenumber-space does not change the results (not shown).

5. The interaction between gravity waves and solar tides

As described above, we consider in this study an iterative approach of the GW-ST interaction (Fig. 1). The propagation of GWs (section 4), on a climatological mean (section 2), is modulated by diurnal tidal fields in the background flow. This leads to a diurnal component in GW momentum and entropy depositions. The STs (section 3) are forced by these depositions. The latter are communicated to the tidal model via Rayleigh-friction and Newtonian-relaxation coefficients, obtained via regression on the GW forcing from the ray-tracer model. With these the tidal model yields modified STs which are then used again in the ray-tracer model for a new simulation of the GW fluxes. This process is iterated until STs and GW fluxes converge. Two different experiments are presented in this work, namely the *"full"* experiment and the *"single-column"* approximation experiment. The converged results of our experiments are shown in subsections 5.2 and 5.3.

5.1. The *"full"* and the *"single-column"* approximation experiments

The *"full"* experiment refers to a simulation with no additional assumption, neither concerning the ray-tracer model nor the tidal model. The effects of horizontal GW propagation and of horizontal background gradients, both in the climate mean and in the STs, are highlighted by a comparison with a simplified *"single-column"* approximation experiment.

The *"single-column"* approximation experiment uses simplifying assumptions common in a conventional parameterization of GW. Note however, that these parameterizations are also employing, on top of a single-column approximation, a steady-state assumption, where an instantaneous equilibrium GW profile is calculated, that one would obtain with time-independent GW source in a steady background. GWs propagate in the *"single-column"* approximation only vertically (see Eq. 10). Horizontal background gradients are neglected and curvature terms are ignored as well (see Eq. 9). The horizontal wavenumber $\mathbf{k}_H$ is kept constant along each ray. Frequency ω and vertical wavenumber m still vary nonetheless, to compensate temporal and vertical spatial changes in the background flow.

In the *"single-column"* approximation experiment, the flux-convergences $f_{x,y,b}$ of the GW depositions (Eq. 18) are then also projected on tidal components and tendencies (see Eqs. 4 and 19) leading to different Rayleigh-friction and Newtonian-relaxation coefficients (altitude-seasonally dependent), used in the linear tidal model.

5.2. Gravity-wave fluxes

We first discuss the flux convergences $f_{x,y,b}$ of the GW momentum and buoyancy depositions (Eq. 18) from the two experiments (Figs. 4 to 6). Daily averaged momentum and buoyancy flux convergences $f_{x,y,b}$ could influence the climatological mean (Fig. 2). In the linear tidal model this effect is, however, not taken into account. The diurnal component

of the GW fluxes acts on the diurnal STs, and also does so in the tidal model. $\|f_x\|_{day}$ is shown in Fig. 5 and $\|f_b\|_{day}$ in Fig. 6. Diurnal STs from the two experiments are presented in subsection 5.3 (Figs. 7 to 10).

From the climatology shown above (section 2), the daily-mean GW forcing is expected to accelerate the climatological mesosphere zonal-wind in the Summer hemisphere, and decelerate it during the Winter hemisphere. As shown in Fig. 4 from the annual cycle and the seasonal altitude-latitude profiles, f_x is accordingly positive in the Summer hemisphere and negative in the Winter hemisphere.

GW acceleration f_x along zonal wind can be approximate by $f_x \approx -\frac{1}{\rho}\partial_r(\rho u'w')$, if one neglects the horizontal divergence of momentum fluxes. Independently, the zonal-momentum fluxes are linked to the horizontal buoyancy fluxes (Eq. 17). Therefore, the zonally averaged buoyancy-flux f_b convergence is linked to the meridional gradient of the zonal-mean vertical horizontal-momentum flux $\partial_\theta(\rho u'w')$. The vertical gradient of the seasonally and zonally averaged zonal-momentum flux $(\rho u'w')$ agrees roughly with the GW seasonal and zonal-mean zonal acceleration f_x (Fig. 4). Its meridional gradient agrees with the buoyancy flux convergence f_b (Fig. 6). The diurnal amplitude of the zonal-momentum flux $\|\rho u'w'\|_{day}$ is, equivalently, linked to the diurnal amplitude of the flux convergences $\|f_x\|_{day}$ and $\|f_b\|_{day}$ (Figs. 5 and 6).

We mention that the GW meridional acceleration f_y (not shown) is slightly stronger than the zonal acceleration f_x. The latitude-altitude distribution of the flux convergences f_x and f_y are similar. How far this is due to the simplified source spectrum used here will be subject of future studies. Radar wind measurements in Hawaii [*Liu et al.*, 2013] show, however, that the diurnal amplitude of the zonal GW acceleration $\|f_y\|_{day}$ is similar, in

amplitude, to its zonal counterpart $\|f_x\|_{day}$. The order of magnitude of these measured fluxes also agrees with those in our model.

Indeed, although our gravity ensemble (subsection 4.2) is idealized, we are still able to reproduce major GW effects on the climatological circulation, for example the seasonal cycle of the daily-mean zonal-mean zonal-acceleration f_x (Figs. 4 and 5).

Concerning the diurnal modulation of the GW deposition, results from the *"full"* and the *"single-column"* approximation experiments are shown together, in order to facilitate easier comparison. In agreement with the results from *Senf and Achatz* [2011], we note a clear rise in diurnal amplitude between the *"full"* experiment and the *"single-column"* approximation experiment.

Likewise the seasonal and zonal-mean daily-mean zonal-acceleration and buoyancy-forcing are considerably stronger in the *"single-column"* experiments (see Figs. 4 to 6). This has been discussed by *Senf and Achatz* [2011]. Meridional refraction of GWs by meridional gradients in the mean zonal wind contribute to an increase in the total GW wavenumber $\|\mathbf{k}\|$, which would have been constant otherwise (if the effect of horizontal gradients are neglected). The increased total wavenumber $\|\mathbf{k}\|$ lead to an increase in intrinsic frequency $\hat{\omega}$ also at higher altitudes which makes the affected GWs slightly less sensitive to wave breaking. Furthermore in the *"full"* experiment, redistribution of GW momentum and buoyancy induced by horizontal propagation additionally reduce the GW forcing [*Senf and Achatz*, 2011].

5.3. Solar tides

The diurnal STs are decomposed following Eq. 1. We restrict ourselves in showing the main components of the diurnal decomposition : the eastward propagating tide DE_3

(zonal wavenumber 3) ; the standing oscillation D_0 ; the sun-synchronous westward propagating tide DW_1 (zonal wavenumber 1) and the westward propagating tide DW_2 (zonal wavenumber 2).

Past studies from Upper Atmosphere Research Satellite (UARS) wind observations [e.g. *Forbes et al.*, 2003; *Forbes and Wu*, 2006; *Zhang et al.*, 2006; *Forbes et al.*, 2007] allow some comparison. No perfect agreement is to be expected, our tidal model being linear. The GW forcing is here approximated by Rayleigh-friction and Newtonian-relaxation coefficients (Eq. 4 and 19 with associate discussions). The coupling between the two kind of waves is only iterative (Fig. 1). Even at this level of simplification, however, the tidal model is able to reproduce important features observed in the seasonal cycle, and the comparison between the two experiments turns out quite instructive.

HAMMONIA tides alongside the results from the *"full"* experiment are shown in Figs. 7 and 8. The annual cycle of tidal amplitudes (Fig. 7) is shown at $95km$, so that a comparison with past observations work is facilitate. Altitude-latitude profiles (Figs. 8 and 9) of annual-mean amplitudes are also presented. Note that the HAMMONIA model uses a classic single-column steady-state GW parameterization. STs in that model are thus affected by the neglect of the effects of horizontal GW propagation and horizontal resolved-flow gradients on the GW fluxes. On the other hand, however, it keeps all nonlinearities of the resolved flow. Differences certainly also came from our idealized GW forcing, as disagreements with observed seasonal cycles differ between tidal components. It is thus a difficult task to associate agreements and disagreements between HAMMONIA STs and our results to specific effects. We refrain from this and show the HAMMONIA results simply for reference.

We here compare ST annual cycles obtained from our linear tidal model in the *"full"* experiment, as those from the HAMMONIA model (both shown in Fig. 7), with observations from *Forbes et al.* [2003, 2007].

• Of DE_3 tidal component, our *"full"* experiment is able to reproduce the two observed equatorial maxima, in November and March. If DE_3 tidal amplitude in the linear model differs from HAMMONIA model and observations, weaker differences in other tidal components' annual cycles are shown.

• Strong similarities are shown in D_0 seasonal cycle between HAMMONIA model and our linear tidal model in the *"full"* experiment. Observed domination of South hemisphere is reproduced.

• Our linear tidal model reveals similar annual cycle of the diurnal migrating tide DW_1 in comparison with HAMMONIA model and observations.

• In the annual cycle of DW_2 component, observed equatorial symmetry is proved also to exist in our tidal model. Amplitude also agrees with observations, but with delayed seasonal variations (approximatively 4 months).

The altitude-latitude profiles (Figs. 8 and 9) exhibit a clear altitude dependence. Likewise some apparent disagreements between observed and modeled seasonal cycle at a given altitude might be due to the same feature occurring at slightly shifted altitudes. The dissipation processes imposed in the upper part of the domain, namely higher than $100 - 110km$ of altitude, certainly explain part of those profiles differences.

Difference between the *"full"* and the *"single-column"* approximation experiments are visible by two means. First, as shown in the previous subsection, the *"single-column"* approximation leads the ray-tracer model to considerably larger momentum and buoyancy

depositions than in the *"full"* configuration. In the *"single-column"* approximation, the rise in amplitude of the GW deposition leads to a clear decrease in the diurnal ST amplitude. This is illustrated in Fig. 9 for two different tidal components, D_0 and DW_2. In Fig. 9, the altitude-latitude profiles of the *"full"* experiment are shown, alongside those same profiles but subtracted with results from the *"single-column"* experiment. Other tidal components also present weaker *"single-column"* ST amplitudes (not shown).

A change in the phase structure is induced by the imaginary parts of the Rayleigh-friction and Newtonian-relaxation coefficients, namely $\gamma^{\mathcal{I}}$ in the previous sections, similar to the effect discussed by *Ortland and Alexander* [2006] (see also Eq. 4 and 19). GW depositions are different between the two experiments, so are thus those forcing-coefficients, and so are then the tidal phase structures. This is visible in Fig. 10 where the sine parts of the DW_1 and DW_2 tides are presented. GWs influence the diurnal migrating DW_1 phase structure and we note a slight increase in the vertical wavenumber of DW_2. The altitude-latitude profile of the sine parts of the meridional velocity of DW_1 and DW_2 tides (from the *"full"* experiment) is shown, alongside the difference between the results of the *"full"* and *"single-column"* experiments. The ST wavelength is thus modified by the GW impact.

6. Summary

GWs and STs contribute, to an important part, to the variability of the middle-atmosphere. They also contribute significantly to the coupling between troposphere and middle-atmosphere. Most often GW dynamics is described in global models via parameterizations. These are based on WKB theory, however, with crucial simplifications. One of these is the *"single-column"* approximation where horizontal GW propagation is neglected

as well as the effect of horizontal gradients in the resolved-scale background through which the GWs propagate. The other simplification is the steady-state assumption, where instantaneous equilibrium profiles for the vertical GW distribution are determined, instead of allowing GWs to vertically propagate at their group velocity. Studies of GW-ST interactions have potentially been affected by these simplifications. *Senf and Achatz* [2011] have shown that they lead to a considerable overestimation of GW amplitudes in the mesosphere and lower-thermosphere (MLT). The feedback of this effect on the tidal structures is the central focus of the present study.

For this purpose we have used two coupled models. The first of these describes the propagation and breaking of GWs on a time and spatially dependent background of a seasonally dependent monthly mean superimposed by STs. GW momentum and entropy fluxes diagnosed from that model are communicated to a linear tidal model. The latter determines new STs which are the used again in the GW model. This is repeated iteratively until the tidal fields converge.

The GW model is a global three-dimensional ray-tracer model, based on the one used by *Senf and Achatz* [2011]. A new phase-space wave-action density conservation scheme [from *Buhler and McIntyre*, 1999b; *Hertzog et al.*, 2002; *Muraschko et al.*, 2014] has been implemented into this model that helps avoiding numerical instabilities likely to occur due to caustics in more conventional approaches [see *Rieper et al.*, 2013]. GWs are described in a spectral type of approach. The spectral density of wave action in phase-space is given by a corresponding phase-space wave-action density that is conserved along trajectories given by group velocity in physical space and WKB wavenumber tendencies in wavenumber space. In a Lagrangian description wave particles (rays) are introduced which transport

the conserved phase-space wave-action density. These are actually representing a small phase-space volume of rays, propagating according to WKB. That volume responds in shape to the local shear of the phase-space velocity.

Along with GW propagation and GW breaking, here described using a static-instability saturation approach, goes a deposition of momentum and buoyancy. This deposition is projected onto diurnal STs fields and their tendencies. Rayleigh-friction and Newtonian-refraction coefficients are calculated from these projections, which are then to be used in the tidal model. Those evaluated coefficients impose in turn a GW forcing on diurnal ST dynamics.

The global three-dimensional dynamics of STs is described by a model obtained by the linearization of a spectral primitive-equation code about a climatological monthly-mean state also allowing for stationary planetary waves [see *Achatz et al.*, 2008]. STs are extracted from the linear tidal model and are then used in a new computation of the GW fluxes in the ray-tracer model. This is iterated a few times to obtain a converged result on GW fluxes and on tidal fields.

Two experiments are performed : the *"full"* and the *"single-column"* approximation experiments. The *"full"* experiment refers to a simulation with no additional assumption, whereas the *"single-column"* approximation experiment refers to the above-described simplification in conventional parameterizations of GWs. An idealized GW source is assumed in both experiments. A lower-boundary is prescribed that is horizontally homogeneous but contains a small ensemble of spectral components with various amplitudes, wavelengths and propagation directions.

Notwithstanding the simplicity of the source, we are able to reproduce important GWs effects on the climatological mean circulation, for example the MLT momentum deposition, daily and zonally averaged. The diurnal components of the deposition of momentum and buoyancy are analyzed, as well as their seasonal cycles. The STs obtained from the coupled system of the ray-tracer and the tidal model compare favorably with observations.

In agreement with the results from *Senf and Achatz* [2011] the amplitudes of the GW momentum and buoyancy depositions are found to be overestimated in the *"single-column"* approximation, an effect which is due to the meridional refraction of GWs originally propagating zonally.

The comparison between the STs from the *"full"* experiment and the *"singe-column"* experiment shows that the larger GW fluxes in the latter lead to weaker tidal amplitudes. Thus, a *"single-column"* approximation entails an underestimation of tidal amplitudes and a different tidal phase structure. An open question remains what effect the simplified description of the GW effect on STs via effective Rayleigh-friction and Newtonian-relaxation has. This is to be addressed in future work by a direct coupling of ray-tracer and tidal models.

Acknowledgments. The data for this paper are available upon request from the authors.

B.R. and U.A. thank the German Federal Ministry of Education and Research (BMBF) for partial support through the program Role of the Middle Atmosphere in Climate (ROMIC) and through grant 01LG1220A. U.A. thanks the German Research Foundation (DFG) for partial support through the research unit Multiscale Dynamics of Gravity Waves (MS-GWaves) and through grants AC 71/8-1, AC 71/9-1 and AC 71/10-1.

703 The authors thank Oliver Bühler and an anonymous referee for their useful comments.

References

704 Achatz, U., N. Grieger, and H. Schmidt (2008), Mechanisms controlling the diurnal so-
705 lar tide: Analysis using a gcm and a linear model, *J. Geophys. Res.*, *113*(A8), doi:
706 10.1029/2007JA012967.

707 Alexander, M. J., et al. (2010), Recent developments in gravity-wave effects in climate
708 models and the global distribution of gravity-wave momentum flux from observations
709 and models, *Q. J. R. Meteorol. Soc.*, *136*, 1103–1124, doi:10.1002/qj.637.

710 Becker, E., and G. Schmitz (2003), Climatological effects of orography and landsea heating
711 contrasts on the gravity wavedriven circulation of the mesosphere, *J. Atmos. Sci.*, *60*,
712 103–118, doi:10.1175/1520-0469(2003)060¡0103:CEOOAL¿2.0.CO;2.

713 Bretherton, F. P., and C. J. R. Garrett (1968), Wavetrains in inhomogeneous moving
714 media, *Proc. R. Soc. A*, *302*(1471), doi:10.1098/rspa.1968.0034.

715 Broutman, D., J. Rottman, and S. D. Eckermann (2004), Ray methods for inter-
716 nal waves in the atmosphere and ocean, *Annu. Rev. Fluid Mech.*, *36*, 233253, doi:
717 10.1146/annurev.fluid.36.050802.122022.

718 Buhler, O., and M. E. McIntyre (1999a), On shear-generated gravity waves that reach the
719 mesosphere. part i: Wave generation, *J. Atmos. Sci.*, *56*, 3749–3763, doi:10.1175/1520-
720 0469(1999)056¡3749:OSGGWT¿2.0.CO;2.

721 Buhler, O., and M. E. McIntyre (1999b), On shear-generated gravity waves that reach
722 the mesosphere. part ii: Wave propagation, *J. Atmos. Sci.*, *56*, 3764–3773, doi:
723 10.1175/1520-0469(1999)056¡3764:OSGGWT¿2.0.CO;2.

Chen, C., D. R. Durran, and G. J. Hakim (2005), Mountain-wave momentum flux in an evolving synoptic-scale flow, *J. Atmos. Sci.*, *62*, 32133231, doi:10.1175/JAS3543.1.

Choi, H.-J., and H.-Y. Chun (2011), Momentum flux spectrum of convective gravity waves. part i: An update of a parameterization using mesoscale simulations, *J. Atmos. Sci.*, *68*, 739–759, doi:10.1175/2010JAS3552.1.

de la Camara, A., and F. Lott (2015), A parameterization of gravity waves emitted by fronts and jets, *Geophys. Res. Lett.*, *42*, 2071–2078, doi:10.1002/2015GL063298.

de la Camara, A., F. Lott, and A. Hertzog (2014), Intermittency in a stochastic parameterization of nonorographic gravity waves, *J. Geophys. Res.: Atmospheres*, *119*, 11,905–11,919, doi:10.1002/2014JD022002.

Dunkerton, T. J., and N. Butchart (1984), Propagation and selective transmission of internal gravity waves in a sudden warming, *J. Atmos. Sci.*, *41*, 14431460, doi:10.1175/1520-0469(1984)041¡1443:PASTOI¿2.0.CO;2.

Eckermann, S. D., and C. J. Marks (1996), An idealized ray model of gravity wave-tidal interactions, *J. Geophys. Res.: Atmospheres*, *101*(D16), 21,195–21,212, doi:10.1029/96JD01660.

Forbes, J., M. Hagan, and X. Zhang (2007), Seasonal cycle of nonmigrating diurnal tides in the MLT region due to tropospheric heating rates from the NCEP/NCAR reanalysis project, *Adv. Space Res.*, *39*(8), 1347–1350, doi:10.1016/j.asr.2003.09.076.

Forbes, J. M., and D. Wu (2006), Solar tides as revealed by measurements of mesosphere temperature by the MLS experiment on UARS, *J. Atmos. Sci.*, *63*, 1776–1797, doi:10.1175/JAS3724.1.

Forbes, J. M., M. E. Hagan, S. Miyahara, Y. Miyoshi, and X. Zhang (2003), Diurnal nonmigrating tides in the tropical lower thermosphere, *Earth, Planets and Space*, *55*(7), 419–426.

Fritts, D. C., and M. J. Alexander (2003), Gravity wave dynamics and effects in the middle atmosphere, *Rev. Geophys.*, *41*(1), doi:10.1029/2001RG000106.

Giering, R., and T. Kaminski (1998), Recipes for adjoint code construction, *ACM Transactions on mathematical software*, *24*(4), 437–474, doi:10.1145/293686.293695.

Grieger, N., G. Schmitz, and U. Achatz (2004), The dependence of the nonmigrating diurnal tide in the mesosphere and lower thermosphere on stationary planetary waves, *JASTP*, *66*(69), 733–754, doi:10.1016/j.jastp.2004.01.022.

Grimshaw, R. (1975), Nonlinear internal gravity-waves in a rotating fluid, *J. Fluid Mech.*, *71*, 497–512, doi:10.1017/S0022112075002704.

Hagan, M. E., and J. M. Forbes (2002), Migrating and nonmigrating diurnal tides in the middle and upper atmosphere excited by tropospheric latent heat release, *J. Geophys. Res.: Atmospheres*, *107*(D24), 1–15, doi:10.1029/2001JD001236.

Hasha, A., O. Buhler, and J. Scinocca (2008), Gravity wave refraction by three-dimensionally varying winds and the global transport of angular momentum, *J. Atmos. Sci.*, *65*, 2892–2906, doi:10.1175/2007JAS2561.1.

Hertzog, A., C. Souprayen, and A. Hauchecorne (2002), Eikonal simulations for the formation and the maintenance of atmospheric gravity wave spectra, *J. Geophys. Res.: Atmospheres*, *107*(D12), 1–14, doi:10.1029/2001JC000815.

Holton, J. R. (1982), The role of gravity wave induced drag and diffusion in the momentum budget of the mesosphere, *J. Atmos. Sci.*, *39*, 791–799, doi:10.1175/1520-

769 0469(1982)039¡0791:TROGWI¿2.0.CO;2.

770 Lindzen, R. S. (1981), Turbulence and stress owing to gravity wave and tidal breakdown,
771 *J. Geophys. Res.: Oceans*, *86*(C10), 9707–9714, doi:10.1029/JC086iC10p09707.

772 Lindzen, R. S., and S. Chapman (1969), Atmospheric tides, *Space science reviews*, *10*(1).

773 Liu, A. Z., X. Lu, and S. J. Franke (2013), Diurnal variation of gravity wave momentum
774 flux and its forcing on the diurnal tide, *J. Geophys. Res.: Atmospheres*, *118*(4), 1668–
775 1678, doi:10.1029/2012JD018653.

776 Liu, H. L., J. M. McInerney, S. Santos, P. H. Lauritzen, M. A. Taylor, and N. M. Pedatella
777 (2014a), Gravity waves simulated by high-resolution whole atmosphere community cli-
778 mate model, *Geophys. Res. Lett.*, *41*, 9106–9112, doi:10.1002/2014GL062468.

779 Liu, X., J. Xu, J. Yue, H. L. Liu, and W. Yuan (2014b), Large winds and wind shears
780 caused by the nonlinear interactions between gravity waves and tidal backgrounds in
781 the mesosphere and lower thermosphere, *J. Geophys. Res.: Space Physics*, *119*(9), doi:
782 10.1002/2014JA020221.

783 McLandress, C. (2002), The seasonal variation of the propagating diurnal tide in the meso-
784 sphere and lower thermosphere. part i: The role of gravity waves and planetary waves, *J.*
785 *Atmos. Sci.*, *59*(5), 893–906, doi:10.1175/1520-0469(2002)059¡0893:TSVOTP¿2.0.CO;2.

786 Meyer, C. K. (1999), Gravity wave interactions with the diurnal propagating tide, *J.*
787 *Geophys. Res.: Atmospheres*, *104*(D4), 4223–4239, doi:10.1029/1998JD200089.

788 Miyahara, S., and J. M. Forbes (1991), Interactions between gravity-waves and the diurnal
789 tide in the mesosphere and lower thermosphere, *J. Meteor. Soc. Japan*, *69*(5), 523–531.

790 Muraschko, J., M. D. Fruman, U. Achatz, S. Hickel, and Y. Toledo (2014), On the ap-
791 plication of wentzelkramerbrillouin theory for the simulation of the weakly nonlinear

792 dynamics of gravity waves, *Q. J. R. Meteorol. Soc.*, doi:10.1002/qj.2381.

793 Ortland, D. A. (2005), A study of the global structure of the migrating diurnal tide using
794 generalized Hough modes, *J. Atmos. Sci.*, *62*(8), doi:10.1175/JAS3501.1.

795 Ortland, D. A., and M. J. Alexander (2006), Gravity wave influence on the global structure
796 of the diurnal tide in the mesosphere and lower thermosphere, *J. Geophys. Res.: Space*
797 *Physics*, *111*(A10), doi:10.1029/2005JA011467.

798 Rieper, F., U. Achatz, and R. Klein (2013), Range of validity of an extended wkb theory
799 for atmospheric gravity waves: one-dimensional and two-dimensional case, *J. Fluid*
800 *Mech.*, *729,*, 330–363, doi:10.1017/jfm.2013.307.

801 Sartelet, K. N. (2003), Wave propagation inside an inertia wave. part i: Role of time
802 dependence and scale separation, *J. Atmos. Sci.*, *60*, 1433–1447, doi:10.1175/1520-
803 0469(2003)060¡1433:WPIAIW¿2.0.CO;2.

804 Schmidt, H., et al. (2006), The HAMMONIA chemistry climate model: sensitivity of
805 the mesopause region to the 11-year solar cycle and co_2 doubling, *J. Climate*, *19*(16),
806 3903–3931, doi:10.1175/JCLI3829.1.

807 Senf, F., and U. Achatz (2011), On the impact of middle-atmosphere thermal tides on the
808 propagation and dissipation of gravity waves, *J. Geophys. Res.: Atmospheres*, *116*(D24),
809 doi:10.1029/2011JD015794.

810 Song, I.-S., and H.-Y. Chun (2005), Momentum flux spectrum of convectively forced
811 internal gravity waves and its application to gravity wave drag parameterization. part
812 i: Theory, *J. Atmos. Sci.*, *62*, 107–124, doi:10.1175/JAS-3363.1.

813 Vadas, S. L. (2013), Compressible f-plane solutions to body forces, heatings, and cool-
814 ings, and application to the primary and secondary gravity waves generated by a

deep convective plume, *J. Geophys. Res.: Space Physics*, *118*(5), 2377–2397, doi: 10.1002/jgra.50163.

Vadas, S. L., and D. C. Fritts (2005), Thermospheric responses to gravity waves: Influences of increasing viscosity and thermal diffusivity, *J. Geophys. Res.*, *110*(D15), doi:10.1029/2004JD005574.

Vadas, S. L., and D. C. Fritts (2006), Influence of solar variability on gravity wave structure and dissipation in the thermosphere from tropospheric convection, *J. Geophys. Res.: Space Physics*, *111*(A10), doi:10.1029/2005JA011510.

Vial, F. (1986), Numerical simulations of atmospheric tides for solstice conditions, *J. Geophys. Res.: Space Physics*, *91*(A8), 8955–8969, doi:10.1029/JA091iA08p08955.

Walterscheid, R. L. (1981), Inertio-gravity wave induced accelerations of mean flow having an imposed periodic component: implications for tidal observations in meteor region, *J. Geophys. Res.*, *86*(C10), 9698–9706, doi:10.1029/JC086iC10p09698.

Walterscheid, R. L., and J. G. De Vore (1981), The semidiurnal atmospheric tide at the equinoxes: A spectral study with mean-wind-related influences and improved heating rates, *J. Atmos. Sci.*, *38*(11), 2291–2304, doi:10.1175/1520-0469(1981)038¡2291:TSATAT¿2.0.CO;2.

Wood, A. R., and D. G. Andrews (1997), A spectral model for simulation of tides in the middle atmosphere. i: Formulation, *JASTP*, *59*(1), 31–51, doi:10.1016/S1364-6826(96)00186-1.

Zhang, X., J. M. Forbes, M. E. Hagan, J. M. Russell, S. E. Palo, C. J. Mertens, and M. G. Mlynczak (2006), Monthly tidal temperatures 20120 km from TIMED/SABER, *J. Geophys. Res.: Space Physics*, *111*(A10), doi:10.1029/2005JA011504.

Figure 1. Sketch of our iterative approach in the study the interplay between GWs and diurnal STs.

Figure 2. Annual cycle (*left*) and June altitude-latitude profiles (*right*) of zonal-mean HAMMONIA data. Shown are the zonal wind (*top row*), the meridional wind (*middle*) and the temperature (*bottom*). Contour interval and starting values in the latitude-altitude profiles are $10m/s$ for the zonal wind, $2m/s$ for the meridional wind and 10^oC for the temperature. Positive (negative) values : black (grey) isolines.

Table 1. GW ensemble used in the ray-tracer model[a]

Number	α	$L_H(km)$	$c_H(m/s)$	$F_H(kg/m/s/day)$
1	0	385	6.79	0.265
2	45	410	6.79	0.317
3	90	504	10.2	0.289
4	135	570	6.79	0.316
5	180	596	6.79	0.370
6	225	570	6.79	0.316
7	270	504	10.2	0.289
8	315	410	6.79	0.317
9	0	385	32.8	0.265
10	45	410	20.4	0.317
11	135	570	20.4	0.316
12	180	596	32.8	0.370
13	225	570	20.4	0.316
14	315	410	20.4	0.317

[a] Abbreviations: α denotes the azimuth angle of the horizontal wave-propagation direction (zero points east and α increases counter-clockwise), L_H is the horizontal wavelength and c_H the horizontal absolute magnitude of the phase velocity. F_H denotes the vertical flux of horizontal momentum at the lower-boundary $\hat{z}_B$ (see subsection 4.3).

Figure 3. Sketch demonstrating the implementation of the GW-source-altitude emission rate. A new ray is initialized in a grid box ones the ray previously initialized there has propagated in the vertical by more than its initial vertical extent. Here this is the case for columns 3, 4, and 6.

Figure 4. The daily-mean of the GW zonal-acceleration f_x. *Top* : annual-cycle (three-monthly moving average), from the ray-tracer *"full"* experiment, vertically averaged between 80 and 90km. Latitude-altitude profiles for northern hemisphere winter (*middle* row) and summer (*bottom*), obtained from the ray-tracer without simplification (*left* column) and in *"single-column"* approximation (*right* column). Positive (negative) values are indicated by black (grey) isolines at $\pm 2^n m/s/day$ with $n = 1, 2, 3 \ldots$

Figure 5. As Fig. 4, but now for the diurnal amplitude of the zonal acceleration.

Figure 6. Latitude-altitude profiles for the buoyancy GW forcing f_b for northern hemisphere winter. The daily-mean (*top*) and the diurnal amplitude (*bottom*) are shown from the ray-tracer without simplification (*left* column) and in *"single-column"* approximation (*right* column). Positive (negative) values are indicated by black (grey) isolines at $\pm 2^n \times 10^{-2} m/s^2/day$ with $n = -1, 0, 1 \ldots$

Figure 7. Seasonal cycle of meridional-wind tidal diurnal amplitudes at $95km$ altitude, in the HAMMONIA model (*left* column) and the linear tidal model in the *"full"* experiment (*right*). Shown are different tidal components. Positive values are indicated by black isolines at $\sqrt{(x/2)^{x/2}}$ m/s with $x = 3, 4, 5 \ldots$ for all components but DW_1 for which $x = 6, 7, 8 \ldots$.

Figure 8. As Fig. 7, but now showing the latitude-altitude profiles of the annual-mean tidal amplitudes.

Figure 9. Latitude-altitude profiles of the diurnal meridional-wind tidal amplitudes. Shown are the annual-mean of tidal components D_0 and DW_2 from the linear tidal model in the *"full"* experiment (*right* panel). The *left* panel shows the amplitude difference between the *"full"* and the *"single-column"* approximation experiments. Positive (negative) values are indicated by black (gray) isolines at $\pm\sqrt{2^{-14,-13,-12\ldots}}$ m/s.

Figure 10. Latitude-altitude profiles of the imaginary (sine) part of the diurnal meridional-wind tides. Shown are the annual-mean of the tidal components DW_1 and DW_2 from the linear tidal model in the *"full"* experiment (*right* panel). The *left* panel shows the field difference between the *"full"* and the *"single-column"* approximation experiments (*left*). Positive (negative) values are indicated by black (gray) isolines at $\pm\sqrt{2^{-14,-13,-12\ldots}}$ m/s.

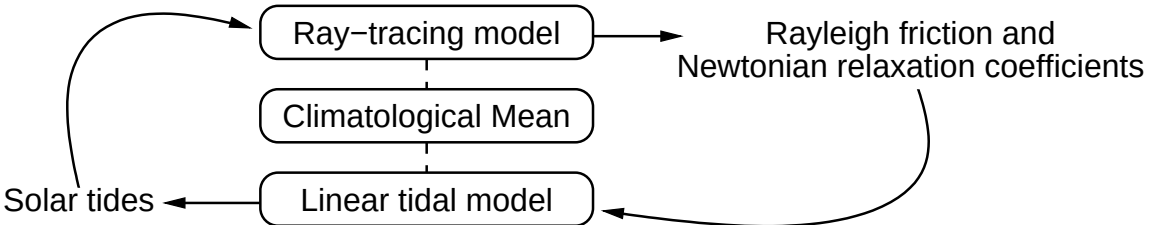
Ray−tracing model
Rayleigh friction and
Newtonian relaxation coefficients
Climatological Mean
Solar tides
Linear tidal model

U_{BG}(lat,time) at z = 60 km

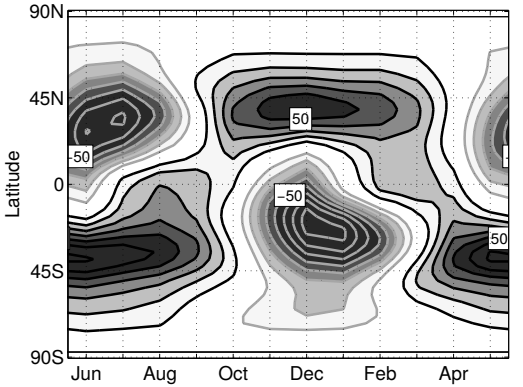

U_{BG}(lat,alt) in June

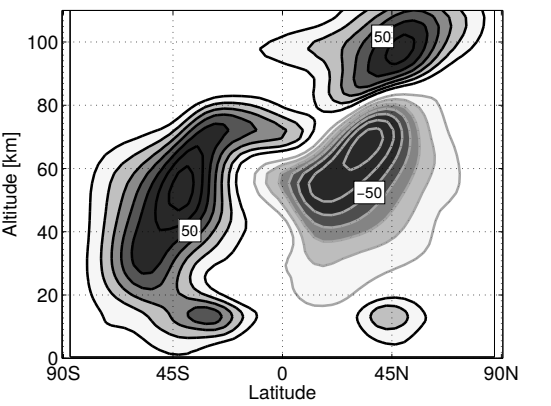

U_{BG}(lat,time) at z = 60 km

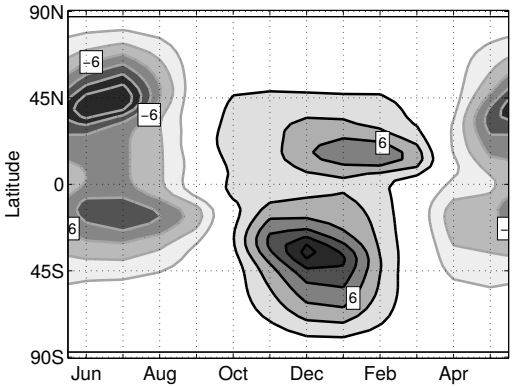

U_{BG}(lat,alt) in June

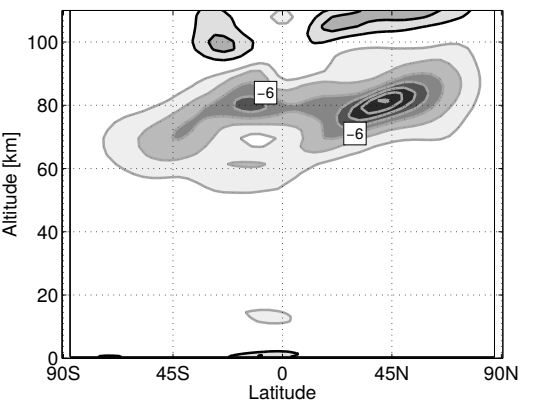

U_{BG}(lat,time) at z = 60 km

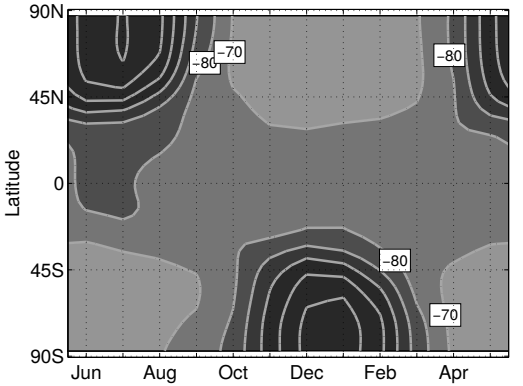

U_{BG}(lat,alt) in June

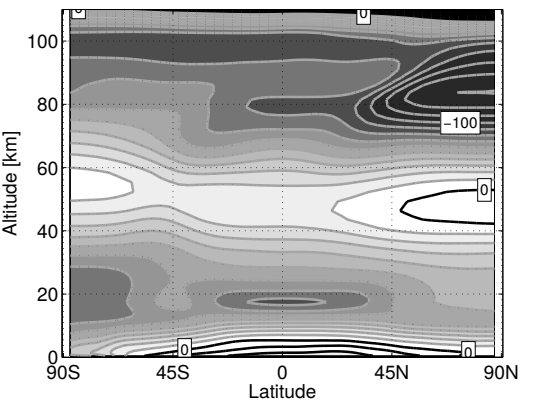

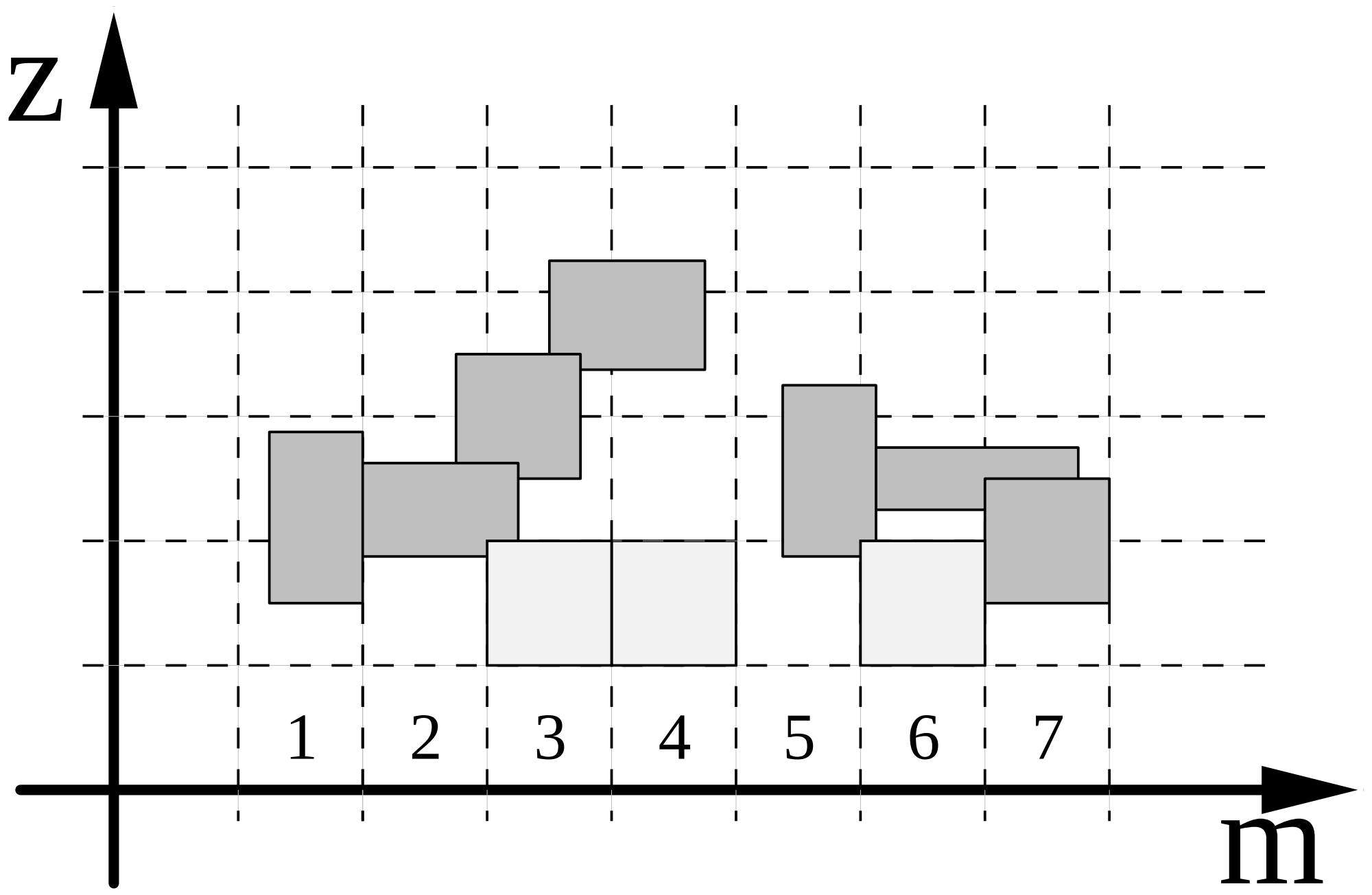
z
1
2
3
4
5
6
7
m

"*Full*" experiment
f_x(lat,time) at 80 < z[*km*] < 90

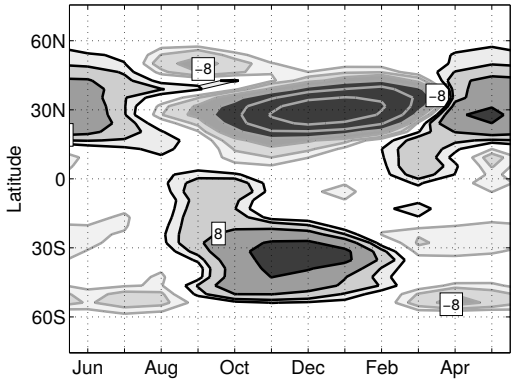

"*Full*" experiment f_x(alt,lat) in DJF "*Single-column*" experiment

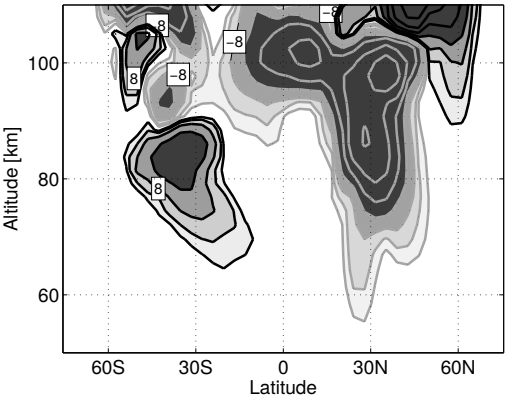

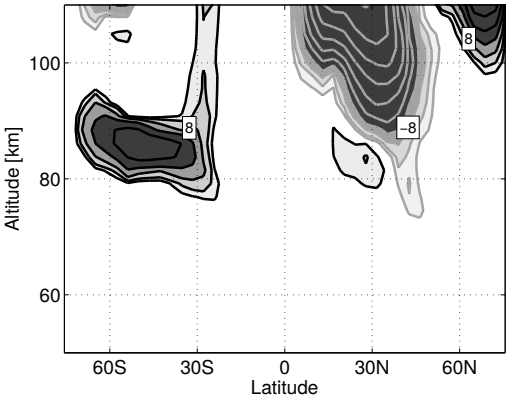

"*Full*" experiment f_x(alt,lat) in MJJ "*Single-column*" experiment

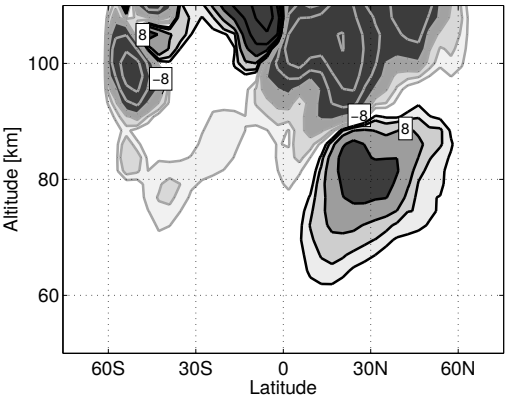

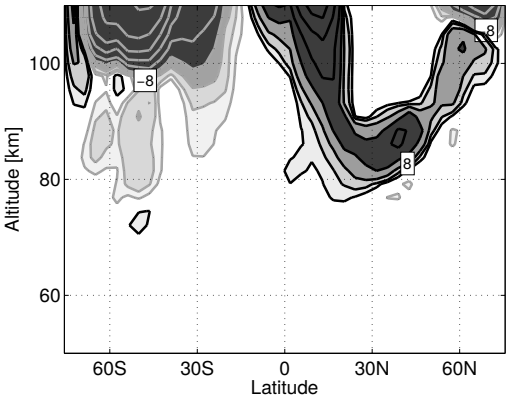

"*Full*" experiment

$||f_x(\text{lat,time})||_{day}$ at $80 < z[km] < 90$

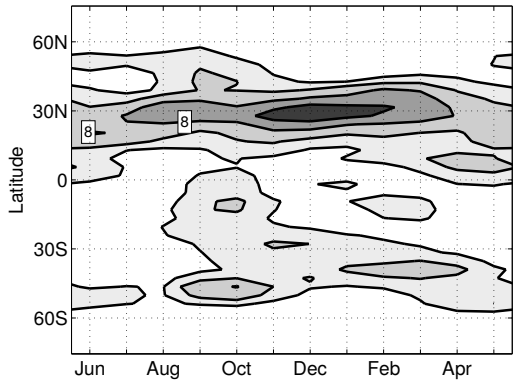

"*Full*" experiment $||f_x(\text{alt,lat})||_{day}$ in DJF "*Single-colunm*" experiment

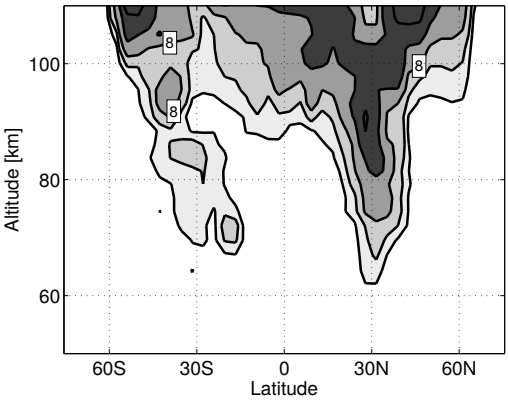

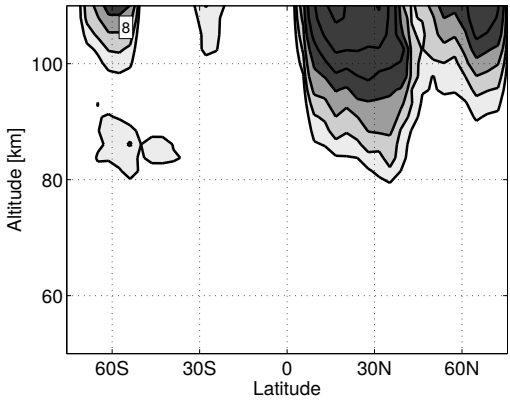

"*Full*" experiment $||f_x(\text{alt,lat})||_{day}$ in MJJ "*Single-colunm*" experiment

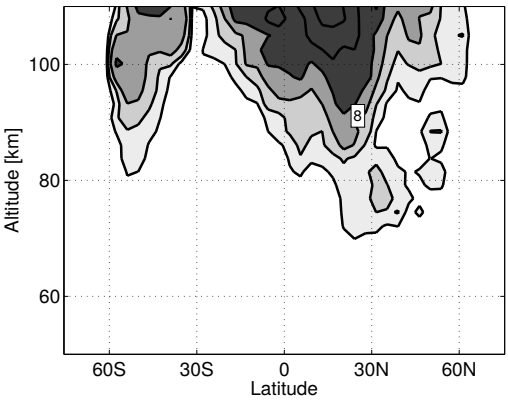

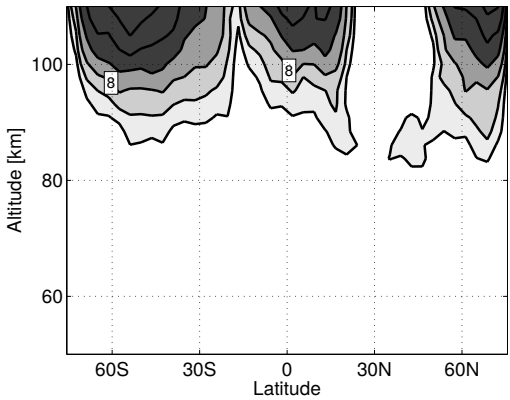

"*Full*" experiment

f_b(alt,lat) in DJF

"*Single-colunm*" experiment

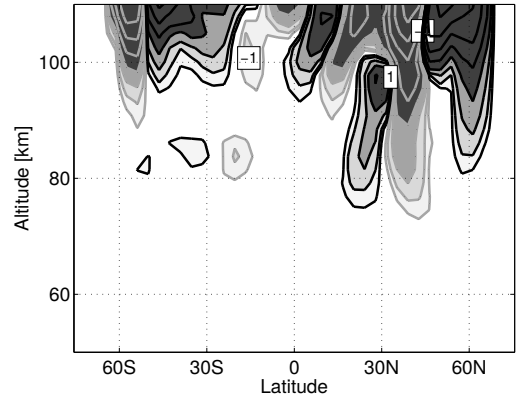

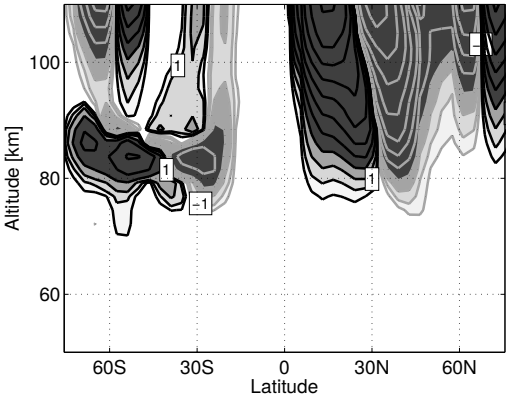

"*Full*" experiment

2 x $||f_b(\text{alt,lat})||_{day}$ in MJJ

"*Single-colunm*" experiment

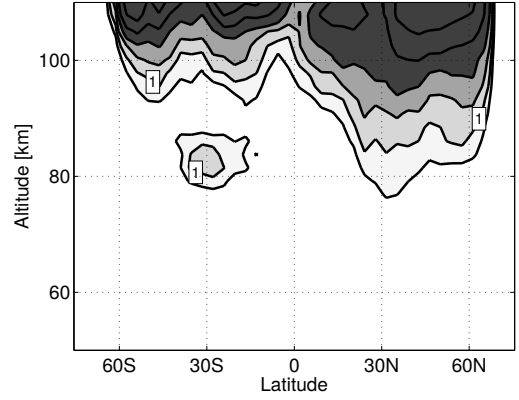

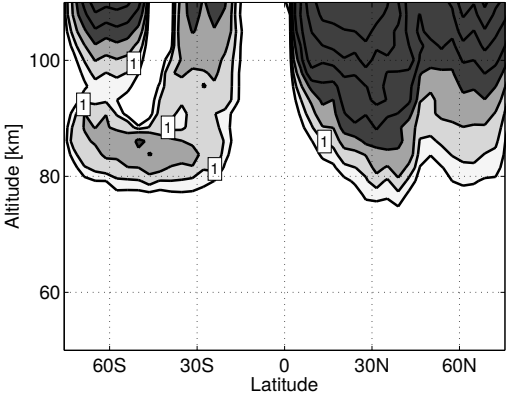

HAMMONIA ||V(lat,time)||$_{day}$ of DE_3 at z = 95 *km* "*Full*" experiment

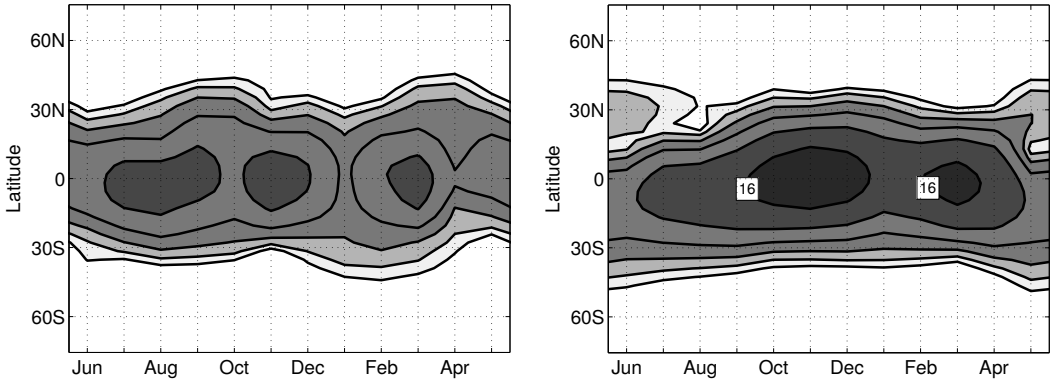

HAMMONIA ||V(lat,time)||$_{day}$ of D_0 at z = 95 *km* "*Full*" experiment

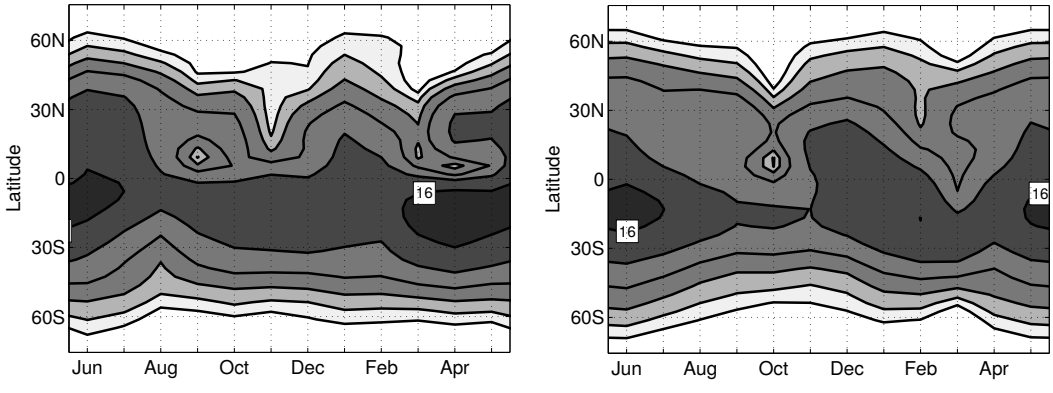

HAMMONIA ||V(lat,time)||$_{day}$ of DW_1 at z = 95 *km* "*Full*" experiment

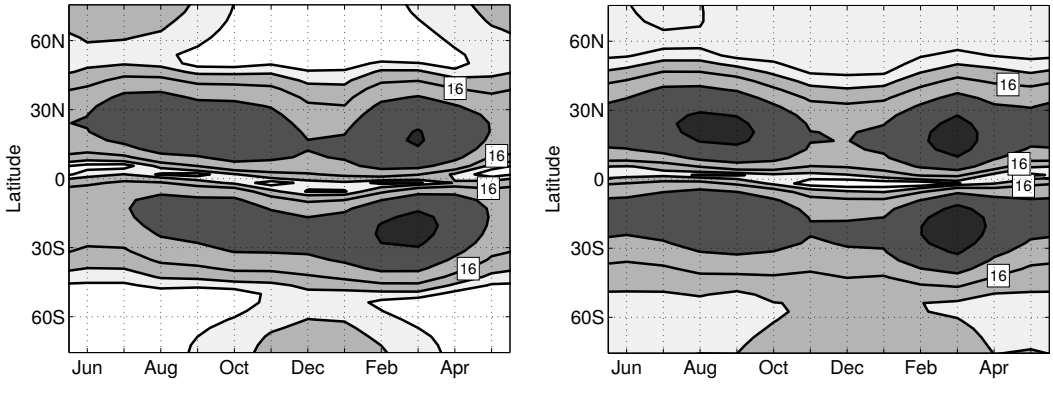

HAMMONIA ||V(lat,time)||$_{day}$ of DW_2 at z = 95 *km* "*Full*" experiment

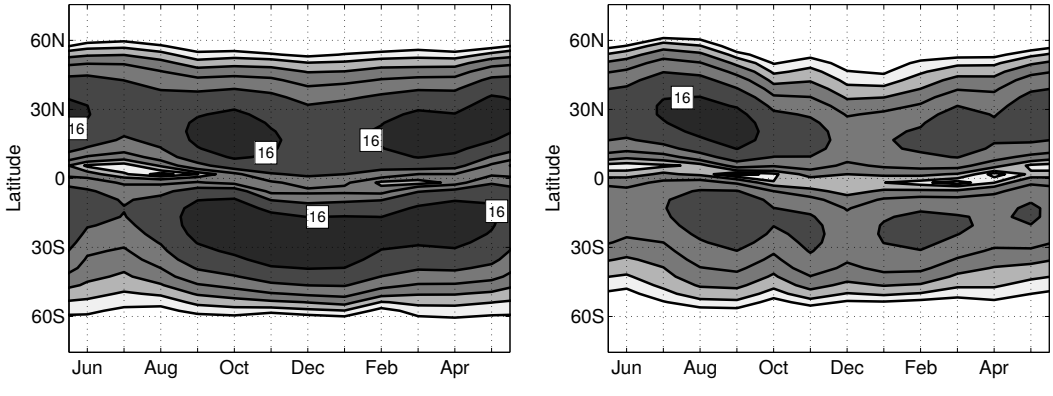

HAMMONIA ||V(lat,alt)||$_{day}$ of DE$_3$ "*Full*" experiment

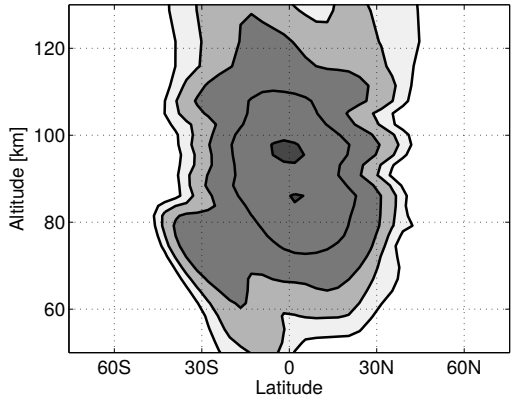

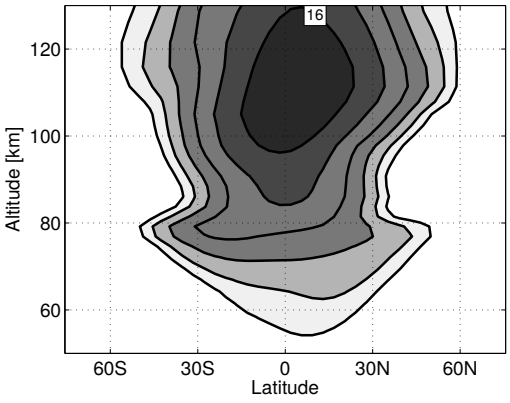

HAMMONIA ||V(lat,alt)||$_{day}$ of D$_0$ "*Full*" experiment

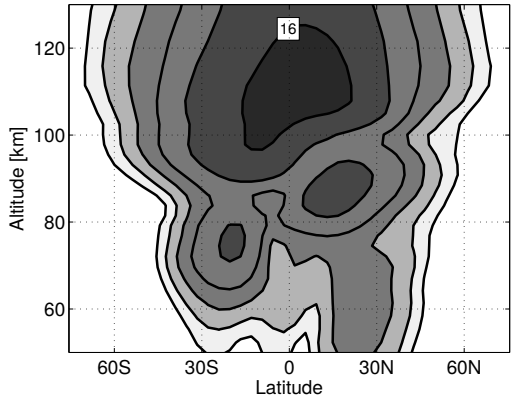

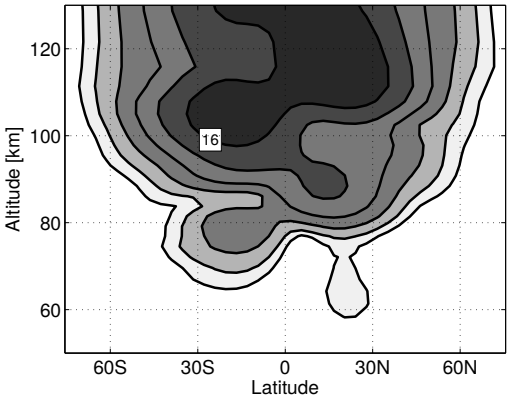

HAMMONIA ||V(lat,alt)||$_{day}$ of DW$_1$ "*Full*" experiment

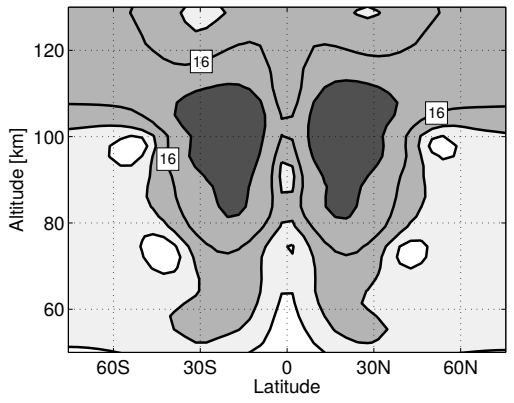

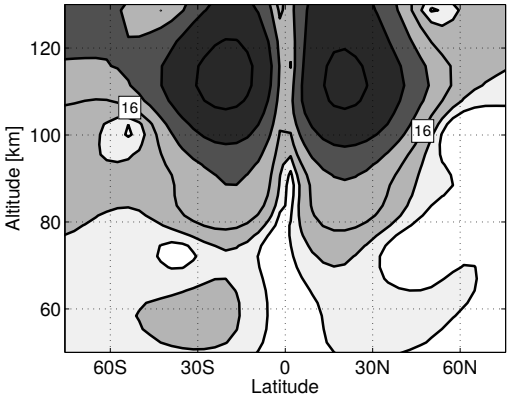

HAMMONIA ||V(lat,alt)||$_{day}$ of DW$_2$ "*Full*" experiment

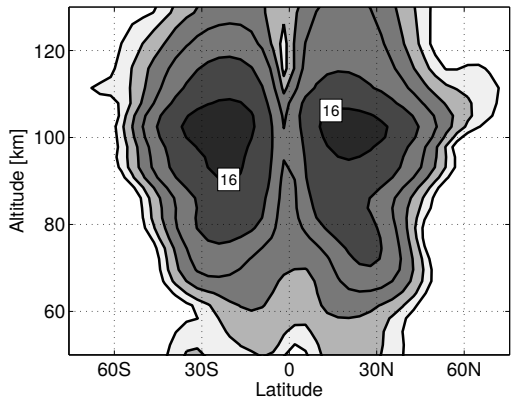

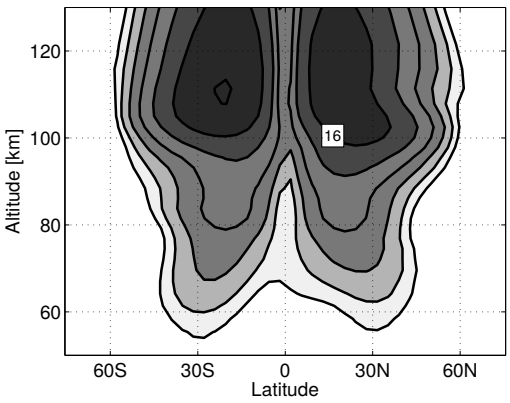

"*Full*" - "*single-column*" experiment ||V(lat,alt)||$_{day}$ of D_0 "*Full*" experiment

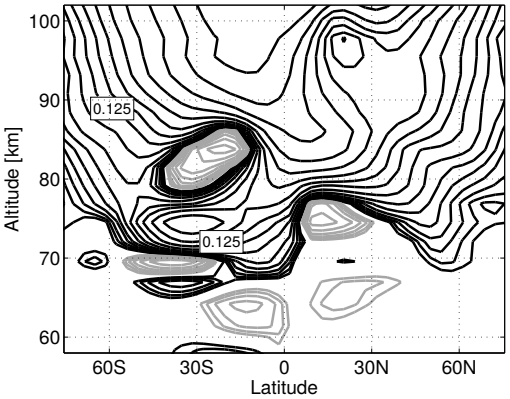

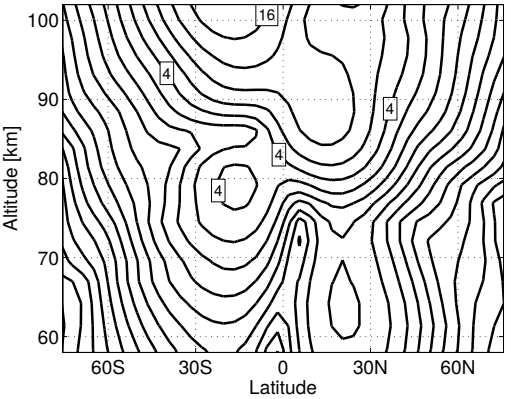

"*Full*" - "*single-column*" experiment ||V(lat,alt)||$_{day}$ of DW_2 "*Full*" experiment

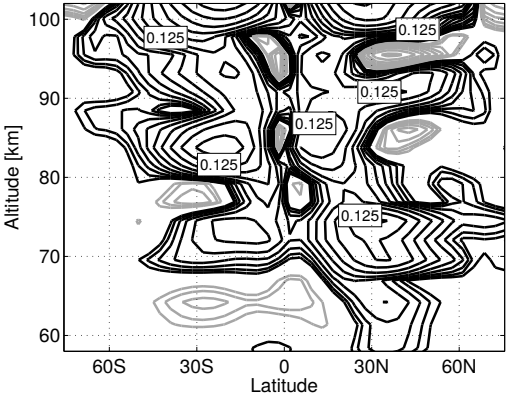

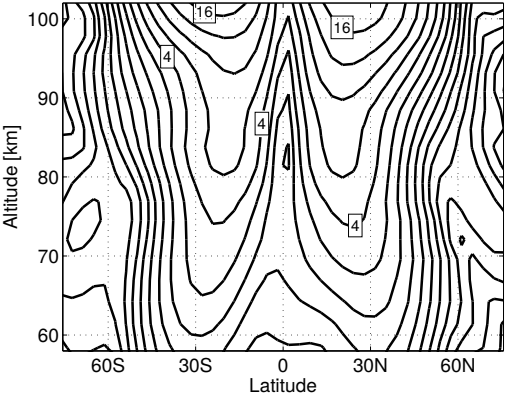

"*Full*" - "*single-column*" experiment $Im(\ V(lat,alt)\ )_{day}$ of DW_1 "*Full*" experiment

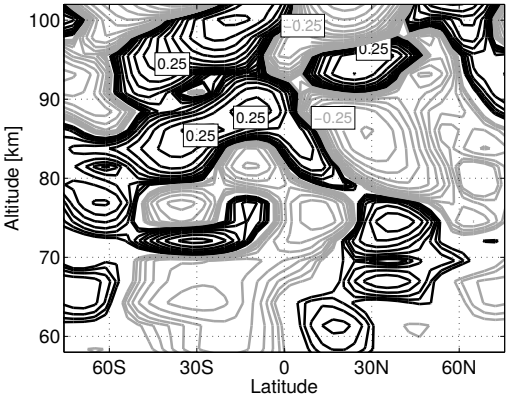

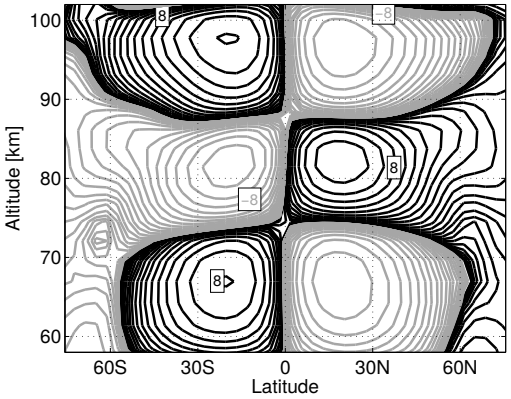

"*Full*" - "*single-column*" experiment $Im(\ V(lat,alt)\ )_{day}$ of DW_2 "*Full*" experiment